Chemical Geology 567 (2021) 120116

Contents lists available at ScienceDirect

Chemical Geology

journal homepage: www.elsevier.com/locate/chemgeo

Progressive ocean oxygenation at ~2.2 Ga inferred from geochemistry and molybdenum isotopes of the Nsuta Mn deposit, Ghana

Kosuke T. Goto [a,*], Yasuhito Sekine [b,c], Takashi Ito [d], Katsuhiko Suzuki [e], Ariel D. Anbar [f,g], Gwyneth W. Gordon [f], Yumiko Harigane [a], Teruyuki Maruoka [h], Gen Shimoda [a], Teruhiko Kashiwabara [e], Yutaro Takaya [a,e,i,j,l], Tatsuo Nozaki [e,i,j,k], James R. Hein [l], George M. Tetteh [m], Frank K. Nyame [m], Shoichi Kiyokawa [n]

[a] Geological Survey of Japan, AIST, Tsukuba, Ibaraki 305-8567, Japan
[b] Earth-Life Science Institute, Tokyo Institute of Technology, Meguro-ku, Tokyo 152-8550, Japan
[c] Institute of Nature and Environmental Technology, Kanazawa University, Kanazawa, Ishikawa 920-1192, Japan
[d] Geosciences Laboratory, College of Education, Ibaraki University, Mito, Ibaraki 310-8512, Japan
[e] Submarine Resources Research Center, Japan Agency for Marine-Earth Science and Technology (JAMSTEC), Yokosuka, Kanagawa 237-0061, Japan
[f] School of Earth and Space Exploration, Arizona State University, Tempe, AZ 85287, USA
[g] Department of Chemistry and Biochemistry, Arizona State University, Tempe, AZ 85287, USA
[h] Graduate School of Life and Environmental Sciences, University of Tsukuba, Ibaraki, Tsukuba 305-8572, Japan
[i] Frontier Research Center for Energy and Resources, The University of Tokyo, Bunkyo-ku, Tokyo 113-8656, Japan
[j] Ocean Resources Research Center for Next Generation, Chiba Institute of Technology, Narashino, Chiba 275-0016, Japan
[k] Department of Planetology, Kobe University, Nada-ku, Kobe, Hyogo 657-8501, Japan
[l] U.S. Geological Survey, PCMSC, Santa Cruz, CA 95060, USA
[m] Department of Earth Science, University of Ghana, P.O. Box LG 58, Legon, Accra, Ghana
[n] Department of Earth and Planetary Science, Kyushu University, Nishi-ku, Fukuoka 819-0395, Japan

ARTICLE INFO

Editor: Michael E. Boettcher

Keywords:
Paleoproterozoic
Oxygen overshoot
Nsuta Mn deposit
Molybdenum isotope
Ocean paleoredox
Geochemistry

ABSTRACT

Recent geochemical data suggest the occurrence of an O_2 overshoot during the mid-Paleoproterozoic (~2.3–2.0 Ga). This O_2 overshoot appears to be consistent with carbon isotope records that suggest high burial rates of organic carbon during that period, the so-called Lomagundi Event. However, little is known about the changes in the ocean redox conditions associated with the O_2 overshoot. To better understand the mid-Paleoproterozoic ocean chemistry, we investigated the microstructures, major and trace element concentrations, Re-Os and Mo ($\delta^{98/95}$Mo) isotopes, and total organic carbon contents of Mn-ore and phyllite samples from the Nsuta Mn deposit in the Birimian Supergroup of Ghana which were deposited during the O_2 overshoot (at ~2.2 Ga). The Mn-ore samples contain early diagenetic rhodochrosite (Mn carbonate). The trace element compositions and Re-Os isotopes of the Mn-ore samples suggest that the rhodochrosite originated from primary manganese oxides (MnO_2) deposited at ~2.2-Ga. The $\delta^{98/95}$Mo values of the least-altered Mn-ore samples range between −1.10‰ and −0.55‰ (relative to NIST3134), suggesting seawater $\delta^{98/95}$Mo values of 1.85 ± 0.18‰ (1SD) during the O_2 overshoot. Such high seawater $\delta^{98/95}$Mo values can be best explained by enhanced removal of isotopically light Mo through adsorption onto Mn oxides. To form extensive Mn-oxide deposits, bottom seawater with O_2 concentrations of > 10 μM would have expanded at ~2.2 Ga. The oxidizing conditions might have supported the emergence of stem group eukaryotes during the mid-Paleoproterozoic.

1. Introduction

Multiple lines of evidence indicate that the first major oxidation of the atmosphere–ocean system occurred between 2.4 and 2.1 Ga (the Great Oxidation Event (GOE); e.g., Holland 2006; Lyons et al. 2014). Recent studies proposed a large fluctuation in the partial pressure of

* Corresponding author.
E-mail address: k.goto@aist.go.jp (K.T. Goto).
[1] Current address: Faculty of Science and Engineering, Waseda University, Shinjuku-ku, Tokyo 169-8555, Japan.

https://doi.org/10.1016/j.chemgeo.2021.120116
Received 12 August 2020; Received in revised form 31 January 2021; Accepted 2 February 2021
Available online 4 February 2021

oxygen (pO_2) during the mid-Paleoproterozoic (~2.3–2.0 Ga); such as, the pO_2 increased from $< 10^{-5}$ to $\sim 10^{-1}$ of the present atmospheric level (PAL) at ~2.3 Ga, then decreased to a much lower level ($< 10^{-3}$–10^{-1} PAL) by ~2.0 Ga, representing an O_2 overshoot (e.g., Bekker and Holland 2012; Hardisty et al. 2014; Kipp et al. 2017; Partin et al. 2013; Planavsky et al. 2012). An increase in the pO_2 during the mid-Paleoproterozoic appears to be consistent with the record of a pronounced positive excursion of the carbon isotopic compositions ($\delta^{13}C$) of up to ~10‰ (the so-called Lomagundi Event), suggesting extensive burial of organic carbon at ~2.3–2.05 Ga (Karhu and Holland 1996; Melezhik et al. 2007). Even though Kipp et al. (2017) recently suggested an expansion of suboxic conditions between 2.3 and 2.1 Ga, there is still inadequate data and/or knowledge of the ocean chemistry during the O_2 overshoot. Considering that fossils of multicellular macro-organisms, possibly stem group eukaryotes, first appeared in the geologic record as early as 2.2 Ga (El Albani et al. 2010, 2014; see also Sawaki et al. (2017) for new age constraints), constraints on the ocean redox conditions during the O_2 overshoot may afford insight into the co-evolution of life and Earth's environments (e.g., Anbar and Knoll 2002).

We recently showed that Mo isotopic compositions ($\delta^{98/95}Mo$) of Fe- and Mn-rich sedimentary rocks, such as modern marine hydrothermal Fe and Mn oxides and ancient iron formations (IFs) composed of Fe- and/or Mn-rich carbonate and/or oxide, provide key information on redox conditions of paleo-oceans (Goto et al. 2020). We can reconstruct the $\delta^{98/95}Mo$ value of the seawater that existed at that time using Fe- and Mn-rich sedimentary rocks, which is a promising proxy indicator to

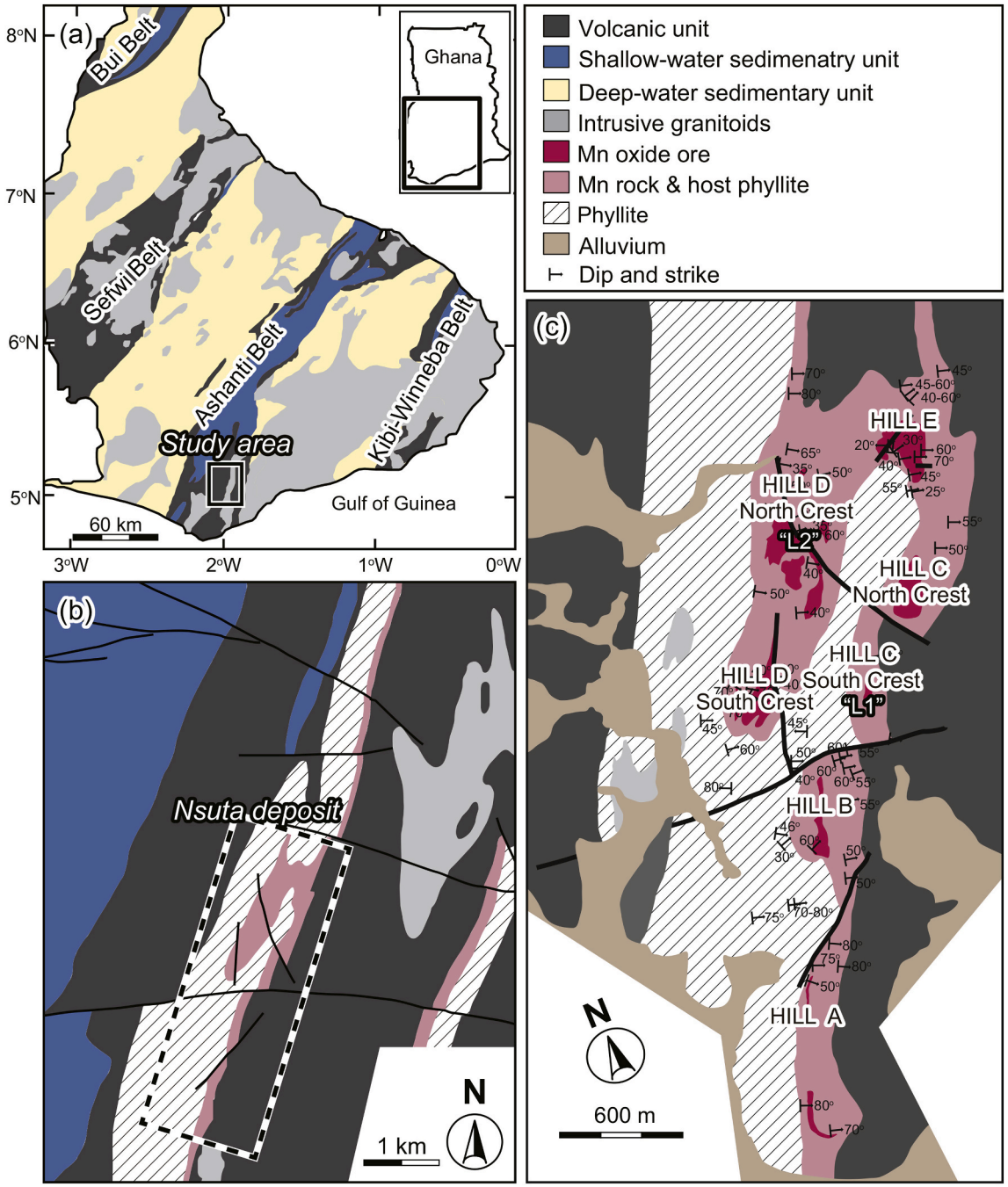

Fig. 1. Simplified geological maps showing the locations of (a) the study area in the Birimian Supergroup, (b) the Nsuta deposit, and (c) Hill C South Crest and Hill D North Crest (referred to as L1 and L2, respectively, in the text) (modified from Dixon 1979).

constrain redox states of the oceans (e.g., Dahl et al. 2010; Siebert et al. 2003). In the present study, we apply this method to ~2.2 Ga Mn-ore samples from the Nsuta Mn deposit of the Birimian Supergroup, Ghana (Fig. 1), aiming to constrain the redox states of the oceans during the O_2 overshoot.

Manganese plays many roles in (bio)geochemical cycles on Earth. Manganese is a redox sensitive element, forming soluble ions under anoxic to suboxic conditions and insoluble oxides under highly oxidizing conditions (Scott and Lyons 2012; Shaw et al. 1990). Geological evidence and biogeochemical model simulations suggest that an increase in the pO_2 from a low level ($< \sim 10^{-5}$ PAL) to a high level ($> \sim 10^{-1}$ PAL) could cause a large perturbation of the ocean Mn cycle (Harada et al. 2015; Kirschvink et al. 2000; Sekine et al. 2011). Such a perturbation may further affect the distribution of bioessential elements because Mn oxide is an effective scavenger of heavy bioessential elements, including Mo, in aquatic systems (e.g., Noda et al. 2019; Shaw et al. 1990).

The $\delta^{98/95}$Mo of the oceans are known to be sensitive to the Mn cycle (e.g., Dahl et al. 2010; Siebert et al. 2003). Analyses of natural samples and laboratory experiments revealed that Mn oxides preferentially remove isotopically light Mo from seawater, resulting in an isotopically heavy reservoir of dissolved Mo in seawater (Siebert et al. 2003; Wasylenki et al. 2008). In addition, Mo is characterized by a long-duration ocean residence time in both the oxic modern ocean (~400 kyr; Miller et al. 2011) and anoxic Paleoproterozoic ocean (~35–140 kyr; Kendall et al. 2011). The $\delta^{98/95}$Mo can thus be used as a tracer of the global ocean Mn cycle during the O_2 overshoot. However, to date, only a small number of $\delta^{98/95}$Mo data exist for Fe- and Mn-rich sedimentary rocks deposited during ~2.35–2.0 Ga, specifically three samples from the ~2.35-Ga iron formations (IFs) of the Pretoria Group in South Africa (Planavsky et al. 2014) and four samples from the ~2.2-Ga Mn-ore of the Francevillian Group in Gabon (Canfield et al. 2013; see also Sawaki et al. (2017) for new age constraints). The ~2.0-Ga Mn-ore from Morro da Mina in Brazil was extensively analyzed for $\delta^{98/95}$Mo values (Cabral et al. 2019), however, those samples had high TOC contents and were metamorphosed to the amphibolite facies, which complicate interpretation of the $\delta^{98/95}$Mo data.

A number of sedimentary Mn deposits occur in Paleoproterozoic greenstone belts of the West African Craton (e.g., in Ghana, Ivory Coast, Burkina Faso, Mali, Eastern Liberia, and Guinea; Markwitz et al. 2016; Maynard 2010; Roy 2006). A large Mn deposit in the Amazonian Craton (the Serra do Navio deposit) is also believed to be laterally equivalent to those in the West African Craton (Chisonga et al. 2012). Because protoores of these Mn deposits likely precipitated on seafloors at ~2.2–2.1 Ga, their geochemical compositions may provide a unique insight into the ocean chemistry during the mid-Paleoproterozoic. In the present study, we obtain the geochemical compositions of phyllite and Mn-ore samples collected from the Nsuta deposit of the Birimian Supergroup in Ghana, which is one of the largest Mn deposits in the West African Craton (Fig. 1). Based on the geochemical data, we constrain the genesis of the Nsuta deposit and examine the local and global ocean redox conditions during the O_2 overshoot.

2. Geological setting

2.1. Birimian Supergroup

The Birimian Supergroup is a Paleoproterozoic volcano-sedimentary succession in the southern part of the West African Craton (Fig. 1a). The supergroup comprises volcanic units and deep- and shallow-water sedimentary units (Grenholm et al. 2019; Leube et al. 1990). These units were intruded by syn- to post-depositional granitoids (Fig. 1a) and have been dated to between ~2.27 to ~1.96 Ga based on U-Pb analyses of magmatic and detrital zircons (e.g., Grenholm et al. 2019; Oberthür et al. 1998). The Birimian Supergroup is considered to have formed in an arc system during an early accretionary phase and subsequent collision phase of what is known as the Eburnean Orogeny (Grenholm et al. 2019). The volcanic units typically occur as multiple NE-SW trending curvilinear units often referred to as volcanic belts (i.e., Bui, Sefwi, Ashanti, and Kibi-Winneba belts; Fig. 1a) (Grenholm et al. 2019; Leube et al. 1990). They consist of mafic-to-felsic volcanic rocks and volcaniclastic and siliciclastic sedimentary rocks (Grenholm et al. 2019; Leube et al. 1990). The volcanic units are separated by isoclinally folded sedimentary units often referred to as sedimentary basins (Grenholm et al. 2019; Leube et al. 1990). The deep-water sedimentary units are predominately composed of pyroclastic rocks, greywacke, and carbonaceous phyllite and have been described as flysch-type deposits (Grenholm et al. 2019; Fig. 1a). The shallow-water sedimentary units are more common in southeastern Ghana and contain siltstone, sandstone, and conglomerate (Grenholm et al. 2019; Fig. 1a). Manganiferous sedimentary rocks are frequently found within the volcanic units or at the boundary between the volcanic and sedimentary units (Dixon 1979; Leube et al. 1990; Melcher 1995) (Figs. 1b and c). Hence, the manganiferous sedimentary rocks were probably deposited on the flanks of volcanic edifices in an arc system (Dixon 1979; Leube et al. 1990). The volcanic and sedimentary rocks in the Birimian Supergroup were metamorphosed to sub-greenschist to amphibolite facies partly due to granitoid intrusions and deformation associated with the Eburnean Orogeny (Grenholm et al. 2019; Leube et al. 1990). However, amphibolite facies metamorphism is only found locally and is interpreted to have been the result of the contact metamorphism due to granitoid intrusions and deformation (Nyame 2013; Nyame et al. 2003).

2.2. Nsuta deposit

The Nsuta deposit is located on the eastern side of the Ashanti Belt and hosted in pyroclastic rocks and/or phyllites (Fig. 1). The Ashanti Belt was intruded by granitoids at ~2.17 Ga (U-Pb zircon age; Oberthür et al. 1998), which thus provides a lower limit of depositional age of the manganiferous sedimentary rocks. Sedimentary rocks from the Nsuta deposit were metamorphosed to greenschist facies, and local supergene alteration is also reported from several outcrops (Dixon 1979; Nyame 2008; Nyame et al. 2003). Mineralogically, three types of Mn-bearing rocks have been reported to occur in the Nsuta deposit; i.e., carbonate (rhodochrosite), silicate (gondite), and oxide (cryptomelane and pyrolusite) rocks. Among these, Mn-carbonate rocks are considered to be the least altered Mn-bearing rocks in the Nsuta deposit. In contrast, Mn silicate and oxide rocks are the products of local metamorphism and oxidative weathering, respectively (Dixon 1979; Nyame et al. 1998).

Based on the mineralogical compositions of Nsuta Mn-ore samples, Mücke et al. (1999) proposed that rhodochrosite was the primary mineral precipitated on the seafloor under reducing and alkaline conditions. However, Nyame et al. (2003) observed micronodule structures in Mn-carbonate samples from the Nsuta deposit and argued that the rhodochrosite in the samples formed during early diagenesis, although its precursor was poorly constrained. The correlative Mn deposit in the Amazonian Craton is considered to have formed by oxidation of dissolved Mn^{2+} (Chisonga et al. 2012). For example, Chisonga et al. (2012) found positive Ce anomalies (Ce/Ce^*_{SN}) in the post-Archean average Australian Shale (PAAS)-normalized rare-earth element (REE) patterns from that deposit. They also reported high concentrations of manganophile elements (e.g., Co, Zn, and Ni) in Mn-carbonate and silicate samples, and posited that the chemical compositions of the samples indicate metal adsorption onto the primary Mn-oxide phases, which were diagenetically transformed into Mn-carbonate and/or silicate minerals.

3. Materials and methods

3.1. Samples

The outcrop samples were collected from two locations within the Nsuta deposit, namely, “Hill C South Crest (hereafter L1)” (5°16′23″N,

1°58′11″W) and "Hill D North Crest (hereafter L2)" (5°16′51″N, 1°58′07″W) (Fig. 1c). The Mn-bearing rocks in both locations exist as Mn-carbonate ore which would be transformed to Mn-oxide ore if the outcrops were influenced by supergene alteration (Dixon 1979). Because the outcrops have been frequently refreshed by mining processes, the influence of modern weathering on the outcrops should be little. The target in both outcrops were Mn-carbonate ore interbedded with pyroclastic rocks (eight samples from L1 and four samples from L2). Also collected from L2 were massive or parallel-laminated phyllite samples separated from the Mn-carbonate layer by ~5 m of pyroclastic rocks. The Mn-ore samples are predominantly composed of rhodochrosite and are usually massive. Approximately 1 mm-thick quartz veins are commonly found in the samples. The microstructure of the Mn-ore samples was further investigated through thin-section observations using an optical microscope and scanning electron microscope (SEM; SU3500, Hitachi) equipped with an energy dispersive X-ray spectrometer (EDS; X-max^{80}, Oxford Instruments) at the Geological Survey of Japan (GSJ). Qualitative chemical compositions of the minerals in the samples were determined using SEM-EDS.

Powdered samples were used for bulk chemical and isotopic analyses of the Mn-ore and phyllite samples. For this purpose, the surface layers of the samples were removed using a diamond-blade saw. The samples were polished with corundum powder to remove contamination derived from the cutter. The polished samples were subsequently washed in an ultrasonic bath with deionized Milli-Q water and dried at ~105 °C. The dried samples were then crushed and pulverized in an agate mortar and pestle. The visible secondary quartz veins were removed before the pulverization. To facilitate the interpretation of geochemical data, bulk mineral compositions of the Mn ore samples were checked prior to the chemical analyses. The mineral compositions of the samples from L1 were partly reported in Yeh et al. (1995), whereas those of the samples from L2 were determined during the present study using an X-ray diffractometer (XRD)(RINT-2500V, Rigaku Co. Ltd) at GSJ (Appendix Table S1).

3.2. Major and trace element analysis

Powdered samples of ~50 mg were weighed in 22-mL PFA vials for digestion. The samples were digested twice using HNO_3 and a mixture of $HClO_4$ and HF, although slight amounts of black materials, most likely organic material, remained undissolved. All the samples were re-dissolved in 0.5 N HNO_3 before measurements. The concentrations of major and trace elements in the solutions were measured using a quadrupole inductively coupled plasma–mass spectrometer (ICP-Q-MS; Agilent 7500cx) at GSJ. Measurement of every two samples was bracketed by the measurement of a matrix-matched calibrated standard solution. A calibrated standard solution was obtained through mixing single- or multi-element standard solutions diluted with 0.5 N HNO_3. This standard bracketing method was used to correct for instrumental drift in the concentration measurements. Interferences from oxides, argides, and doubly-charged ions were corrected based on estimating formation rates through a series of synthesized standard analyses. The standard analyses were conducted on the same day as the sample analysis. In addition to the collected samples, we also analyzed geochemical reference materials of basalt (JB-2; GSJ) and Mn nodule (Nod P-1; United States Geological Survey (USGS)) (Appendix Table S2).

3.3. Re-Os isotope analysis

Powdered samples weighing ~1 g were added into Carius tubes together with ^{190}Os- and ^{185}Re-enriched spike solutions and a dissolution medium. Two types of dissolution media were used for the analysis depending on the rock type; 6 mL of inverse *aqua regia* was used for the Mn-ore samples, and 8 mL of CrO_3-H_2SO_4 for the phyllite samples. After sealing the tubes, those containing inverse *aqua regia* were heated for 24 h at 220 °C (Kato et al. 2005), while those containing CrO_3-H_2SO_4 were heated for 48 h at 240 °C (Selby and Creaser 2003). Osmium and Re were separated with CCl_4 solvent extraction (Cohen and Waters 1996). The Os in the CCl_4 solution was back-extracted using HBr and further purified with micro-distillation (Birck et al. 1997). The Re that remained in the inverse *aqua regia* or CrO_3-H_2SO_4 solution was separated through a two-stage ion-exchange method using an anion resin (Muromac® AG1X-8, 100–200 mesh, Muromachi Chemical Inc.). The purified samples were loaded onto Pt filaments with a $Ba(NO_3)_2$ activator. The isotopic compositions of Re and Os were measured using a negative thermal ionization mass spectrometry (N-TIMS; Thermo Finnigan TRITION) at Japan Agency for Marine-Earth Science and Technology. In addition to the collected samples, we also analyzed geochemical reference materials of Mn nodule (JMn-1; GSJ) and silty marine shale (SCo-1; USGS) (Appendix Table S3). All measurement data were corrected for procedural blank levels of ~12 pg for Re, ~2 pg for Os, and ~0.2 for ^{187}Os/^{188}Os.

3.4. Mo isotope analysis

The Mo isotope analysis of the Mn-ore samples was conducted using methods described by Gordon et al. (2009) and Romaniello et al. (2016). The phyllite samples were not analyzed because they generally exhibited low Mo concentrations (< 1 ppm; Appendix Table S2). The samples were leached using 6 N HCl, which selectively, but not completely, dissolved carbonate minerals, and minimized the contributions of Mo derived from detrital and organic materials, although the mineral compositions of the residues were not identified. For comparison, we also tested digestion using HNO_3 and HF: i.e., HNO_3-HF-$HClO_4$ digestion for the L1 samples and HNO_3-HCl-HF digestion for the L2 samples. The samples were analyzed at GSJ except for the L2 samples digested using HNO_3-HCl-HF which were analyzed at the W. M. Keck Foundation Laboratory for Environmental Biogeochemistry at Arizona State University. Supernatants containing ~500 ng of Mo were transferred into 22-mL PFA vials and then mixed with a calibrated ^{97}Mo–^{100}Mo-spike solution. Molybdenum was separated from the matrix with a two-stage ion-exchange method using an anion resin (AG1X-8, 100–200 mesh, Bio-Rad Laboratories) and a cation resin (AG50WX-8, 200–400 mesh, Bio-Rad Laboratories). The isotopic compositions of the samples were analyzed using a multicollector ICP-MS (Neptune, Thermo Fisher Scientific). All the samples were measured in triplicate and the mean values reported. The isotopic compositions were expressed using conventional delta notation relative to NIST SRM 3134, as follows: $\delta^{98/95}Mo = ({}^{98/95}R_{sample} / {}^{98/95}R_{NIST\ SRM\ 3134} - 1) \times 1000$, where $^{98/95}R$ is the ^{98}Mo/^{95}Mo ratio. Geochemical reference materials (Nod A-1 and Nod P-1; USGS) were also analyzed along the samples (Appendix Table S4).

3.5. Total organic carbon analysis

For total organic carbon (TOC) content analysis, Mn-ore samples weighing ~300–600 mg were first treated with 6 N HCl at 80 °C for ~3 days to remove carbonate minerals. The residues were rinsed three times with deionized Milli-Q water and then dried at 110 °C overnight. The residual fractions, mostly silicate minerals, accounted for 2–11 wt% of total sample amounts for the L1 samples and 10–39 wt% of those for the L2 samples (Appendix Table S5). Portions of the dried samples weighing ~1–4 mg were placed in tin cups. Their carbon isotopic ratios were measured using an elemental analyzer/isotope ratio mass spectrometer (EA/IRMS) system (Isoprime-EA, Isoprime Ltd.) at the University of Tsukuba. Some of the Mn-ore samples were also measured for bulk isotopic ratios. The TOC contents were determined through calibration of the ion currents using $m/z = 44$ in the IRMS. The carbon isotopic compositions (i.e., $\delta^{13}C$) of organic materials in the samples with high TOC contents and of bulk samples were also determined during the measurement. The isotopic compositions were expressed using conventional δ notation relative to the V-PDB (Vienna-Pee Dee Belemnite) reference value; $\delta^{13}C = ({}^{13}R_{sample} / {}^{13}R_{standard} - 1) \times 1000$, where ^{13}R is the ^{13}C/^{12}C ratio. The measurements were performed in quadruplicate

for each sample and the average concentrations and isotopic compositions were adopted. The analytical uncertainties were expressed as one standard deviation of the measurements (Appendix Table S5).

4. Results and discussion

The geochemical data (major and trace element concentrations, Re-Os isotopes, $\delta^{98/95}$Mo, TOC, δ^{13}C) are summarized in Appendix Tables S2–S5. Here, we first describe the results of microscopic observations and Re-Os dating to consider the influence of the post-depositional alteration processes (Sec. 4.1). We then use the trace element data to explore the local redox conditions during formation of the Nsuta deposit (Sec. 4.2). Finally, we show the results of the $\delta^{98/95}$Mo analysis and discuss the global ocean redox conditions existed during the mid-Paleoproterozoic based on the framework proposed in Goto et al. (2020) (Sec. 4.3).

4.1. Microscopic observations and Re-Os dating: Potential effects of post-depositional alteration

The microscope and SEM-EDS data indicate that the Mn-ore samples collected from both outcrops (L1 and L2) are predominately composed of anhedral rhodochrosite with the grain diameter of ~25–50 μm (Fig. 2). Some rhodochrosite grains coalesced into large aggregates (Figs. 2a–c, g). Minor amounts of silicate minerals (quartz and aluminum silicates) also occur in the samples. Sulfide minerals were rarely found during the thin section observations, although those minerals were previously reported from Mn-carbonate rocks of the Nsuta deposit (Mücke et al. 1999). The results of the microscope observations are supported by the XRD data (Appendix Table S1). Backscattered electron (BSE) images show concentric features or zoning within the rhodochrosite grains (Figs. 2c and g). In samples from L1, the zonation seems to coincide with variations in the Mg content (Figs. 2c–f). In contrast, in the L2 samples, the zonation corresponds to Ca content variations (Figs. 2g–j). Similar zonation has been observed in the Mn-carbonate rocks collected from other outcrops of the Nsuta deposit (Nyame et al. 2003) and Phanerozoic marine sediments (Chow et al. 2000; Johnson et al. 2016). These features of rhodochrosite grains may reflect their diagenetic precipitation within sediments (Chow et al. 2000; Nyame et al. 2003) and/or early diagenetic production from primarily Mn oxides (Johnson et al. 2016). Calcium-rich rhodochrosite cements are also frequently observed in the L2 samples (Fig. 2i), whereas such cements rarely occur in the L1 samples (Fig. 2e).

In agreement with the SEM-EDS observation, the Ca/Mg and Ca/Mn ratios of the Mn-ore samples are significantly variable between the sampling sites. The L2 samples exhibit higher Ca/Mg and Ca/Mn ratios (Ca/Mg = 4.9–10.4 wt%/wt%, Ca/Mn = 0.25–0.46 wt%/wt%) than those of the L1 samples (Ca/Mg = 0.47–0.91 wt%/wt%, Ca/Mn = 0.03–0.08 wt%/wt%) (Fig. 3). The residual fractions after HCl digestion, mostly silicate minerals, were generally low (Appendix Table S5), especially for the L1 samples that were 2–11 wt% of the total sample. Hence, the Ca/Mg and Ca/Mn ratios of the samples mostly reflect those of rhodochrosite minerals rather than those of detrital silicates. The Ca/Mg ratios of the L1 samples are within the range of suggested Cenozoic seawater (Ca/Mg = 0.3–1.7 wt%/wt%; Coggon et al. 2010) (Fig. 3a), in contrast to the Ca/Mg ratios of the L2 samples, which are significantly higher. Because Ca is effectively released from basalts, volcanic ash, and igneous components of terrigenous material during warm/high temperature alteration (> ~20 °C), hydrothermal fluids that leach these igneous materials typically exhibit higher concentrations of Ca than seawater (e.g., Coogan and Gills, 2018; Wheat and Mottl 2000). In contrast, Mg can be depleted in hydrothermal fluids due to the formation of secondary minerals (Coogan and Gills, 2018; Wheat and Mottl 2000). Previous experimental investigations showed that the Ca/Mn ratios of Mn-rich carbonate minerals broadly reflect Ca and Mn contents of the source solutions (Böttcher 1998; Mucci 2004). Hence, if the rhodochrosite from both outcrops is of early diagenetic origin (Nyame et al. 2003), the difference in the Ca/Mg and Ca/Mn ratios suggests spatial chemical heterogeneity of the pore water during formation of rhodochrosite. The heterogeneity of pore-water chemistry may reflect the variable contributions of hydrothermal fluids. The high Ca/Mg ratios of the L2 samples suggest that they were more affected by hydrothermal fluids than the L1 samples, which may be consistent with the occurrence of Ca-rich cements in the L2 samples (Fig. 2i). This interpretation is also supported by larger positive Eu anomalies of the L2 samples (Eu*/Eu = 1.4–2.2) compared to the L1 samples (Eu*/Eu = 1.0–1.5) in PAAS-normalized REE patterns (Bau 1991; Fig. 4a). Alternatively, the difference in the Ca/Mg and Ca/Mn ratios may reflect different origins of rhodochrosite from L1 and L2. Rhodochrosite in L1 could have precipitated from seawater (Mücke et al. 1999), whereas that in L2 could have formed from hydrothermal fluids.

We further evaluate the timing of the potential influence of hydrothermal fluids based on the Re-Os isotope data (Figs. 4 and 5). With the exception of a few Mn-ore samples that possess high Os contents (Figs. 4c and d), the analyzed samples generally exhibit low Re and Os concentrations compared with upper continental crust (~200–600 pg/g for Re and ~12–20 pg/g for ^{192}Os; Peucker-Ehrenbrink and Jahn 2001), which seems to be consistent with the absence of sulfide minerals in the analyzed samples. The Re-Os isotopic compositions of all of the phyllite and Mn-ore samples from both outcrops yield a single isochron with an age of 2235 ± 64 Ma and an initial ^{187}Os/^{188}Os ratio of 0.22 ± 0.03 (Fig. 5). If post-depositional fluids affected the analyzed samples, the Re-Os age should have been attributed to the incorporation and/or removal of Re and Os. Because of the uncertainty in the Re-Os age probably resulted from detrital inputs of Re and Os, we cannot rule out contributions of post-depositional fluids immediately after the deposition. However, the isochron age is consistent with the putative depositional age of the Nsuta deposit (> 2.17 Ga), constrained by U-Pb zircon ages of intrusive granitoids in the Ashanti Belt of the Birimian Supergroup (Oberthür et al. 1998). The Re-Os age may be also supported by the high δ^{13}C of organic material in the Mn-ore samples (−19 to −14‰; Appendix Table S5), suggestive of an association with the Lomagundi Event that occurred between ~2.3–2.05 Ga (Karhu and Holland 1996; Melezhik et al. 2007). Hence, the Re-Os data indicate that little overprinting or disturbance by young (e.g., < ~2.2 Ga) metamorphic and alteration events, including modern supergene alteration, affected the samples studied here.

4.2. Trace element compositions: Local redox conditions

The petrographic observations and Re-Os isotope data indicate that (1) rhodochrosite is the dominant mineral in the Mn-ore samples, (2) chemical compositions of the rhodochrosite may have been partly influenced by hydrothermal fluids and, (3) the rhodochrosite could be an early diagenetic product or a primary precipitate formed at ~2.2 Ga. Given the redox-sensitive behavior of Mn (e.g, Scott and Lyons 2012; Shaws et al., 1990), a constraint on a possible precursor of the rhodochrosite may provide insight into the local redox conditions. Petrographic observations often allow multiple interpretations of a possible precursor (e.g., Nyame et al. 2003). Hence, to constrain the origins of the rhodochrosite, we focus on the trace element compositions of the samples (Fig. 4). Although the chemical compositions may have been affected during early diagenesis, any pattern of enrichment/depletion of trace elements preserved in the Mn-bearing phases can provide a clue to trace the primary mineral compositions.

Our results show that the Mn-ore samples collected from both outcrops are enriched in several manganophile elements (Ni, Zn, and Mo) compared to the phyllite samples, although Cr enrichment is absent (Figs. 4e–h). In addition, the Mn-ore samples are characterized by high Os and low Re concentrations (Figs. 4c and d), resulting in the low Re/Os ratios (Fig. 5). The patterns of the trace elements resemble those of modern sediments containing Mn oxides (MnO_2) (e.g., Barrett et al.

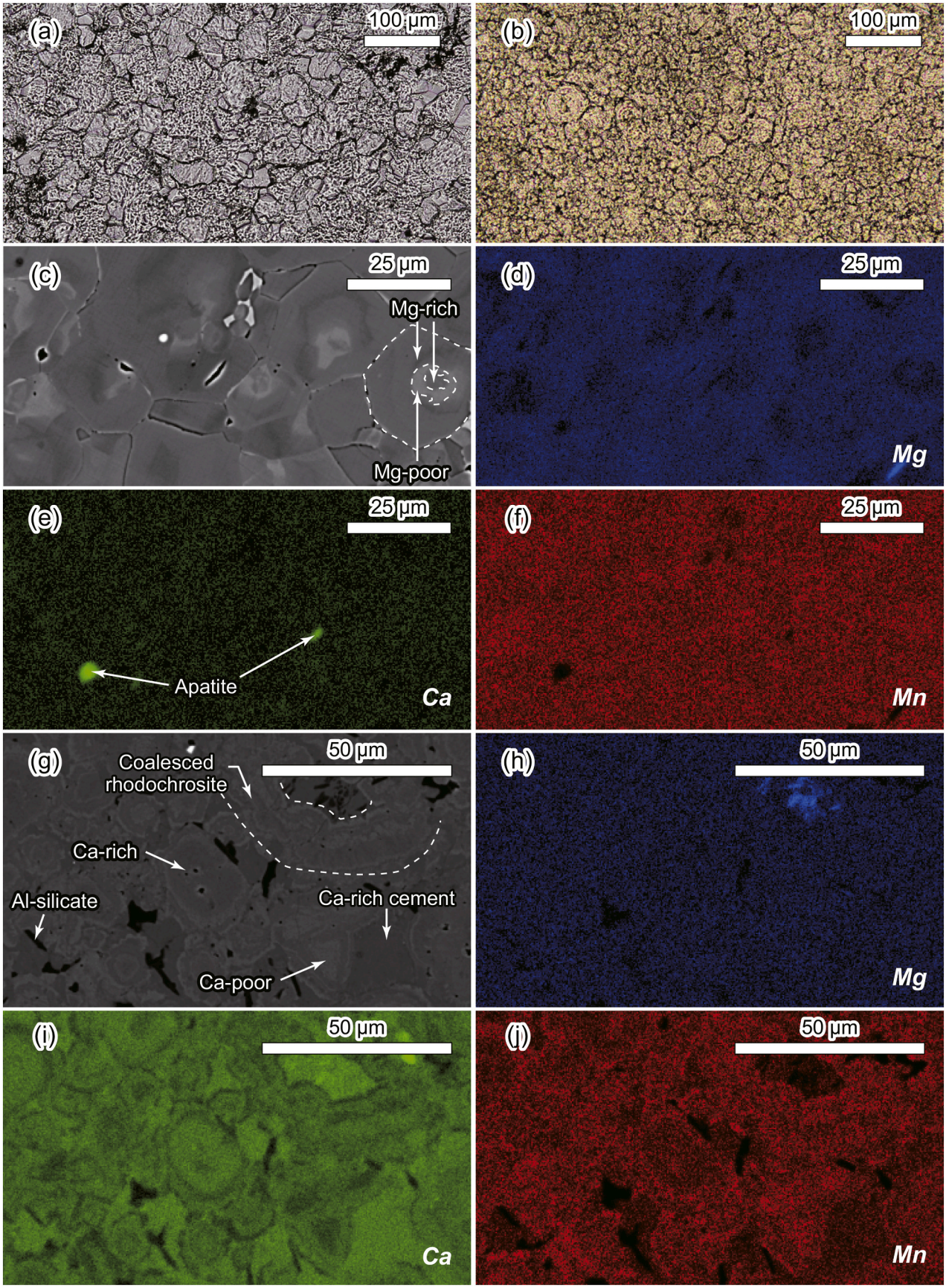

Fig. 2. Representative photomicrographs, BSE images, and elemental maps of Mn-carbonate ore samples taken from the Nsuta deposit. Photomicrographs in plane-polarized light of samples taken from (a) L1 (993–29–1B) and (b) L2 (NA17). BSE images and elemental maps of samples taken from (c–f) L1 (993–29–1B) and (g–j) L2 (NA17). Ca-rich minerals in (e) are tentatively identified as apatite from the elemental mapping data.

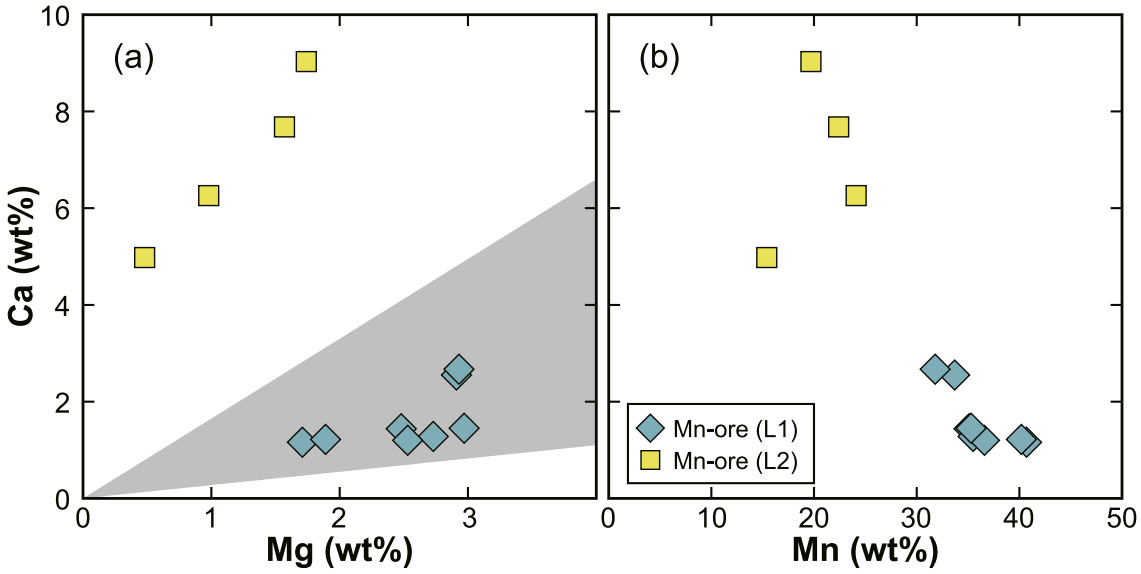

Fig. 3. Crossplots of (a) Ca and Mg and (b) Ca and Mn concentrations in Mn-ore samples taken from the Nsuta deposit. The shaded region indicates the range of the Ca/Mg ratios of Phanerozoic seawater (Coggon et al. 2010).

1987; Peucker-Ehrenbrink et al. 1995; Manceau et al. 2007), and are consistent with the co-enrichment patterns of trace elements adsorbed onto Mn oxides (δ-MnO_2) determined experimentally (Noda et al. 2019). The abundance of manganophile elements normalized by Mn concentrations in the analyzed samples (~3–14 μg/g/wt% for Zn, ~2–7 μg/g/wt% for Ni, and ~0.3–8 μg/g/wt% for Mo) tends to be lower than those in modern sediments (~40–110 μg/g/wt% for Zn, ~50–170 μg/g/wt% for Ni, and ~5–30 μg/g/wt% for Mo; Barrett et al. 1987). The relatively small amounts of manganophile elements in the Nsuta samples may reflect low concentrations of those elements in mid-Paleoproterozoic seawater compared with modern seawater (Scott et al. 2008; Large et al. 2014). Alternatively, a part of manganophile elements could have been released from the Nsuta deposit during early diagenesis (e.g., Atkins et al. 2014).

We also find obvious positive Ce anomalies ($Ce^*/Ce > 1.05$) in the PAAS-normalized REE patterns of all the Mn-ore samples, whereas such anomalies are rarely observed in the phyllite samples (Fig. 4b). The REE patterns of the phyllite samples probably reflect that of the rocks eroded in the area. Chisonga et al. (2012) also found positive Ce anomalies for samples collected from the Serra do Navio Mn deposit, which is considered to be a lateral and temporal correlative of the Nsuta deposit. In contrast to these positive anomalies, Nyame (2008) reported negative or no Ce anomalies for Mn-carbonate samples collected from the Nsuta deposit. In modern oxygenated oceans, a certain fraction of dissolved Ce (III) is oxidized to immobile Ce (IV) on the surface of MnO_2 (Bau et al. 2014; Takahashi et al. 2007). This process can cause a positive Ce anomaly in the REE pattern of Mn oxides. Since the phyllite samples show no clear positive Ce anomalies, the decoupling of Ce from other REEs in the Nsuta deposit likely reflects the oxidative scavenging of Ce by Mn oxides. A positive Ce anomaly in Mn-carbonate ores is often considered key evidence for a hydrogenetic Mn-oxide precursor (e.g., Hein et al. 1999; Polgari et al., 2012). The absence of clear positive Ce anomalies in Mn-ore samples from other outcrops (Nyame 2008) implies that the magnitude of this anomaly in the Nsuta samples was also affected by the accretion rate of the oxides which can be influenced by local depositional settings (Bau et al. 2014; Kuhn et al. 1998).

To summarize, the trace element compositions of the Mn-ore samples share many features with modern Mn oxide (MnO_2) samples, although the studied samples are now predominantly composed of rhodochrosite (Sec. 4.1). These observations suggest that Mn oxides were the precursor of rhodochrosite from the L1 and L2 Nsuta outcrops. Considering the Re-Os isotope data (Fig. 5; Sec. 4.1), the original Mn oxides were most likely precipitated on the seafloor at ~2.2 Ga and transformed to rhodochrosite through burial diagenesis. Negative $\delta^{13}C$ values of the bulk samples, ranging from −13 to −4‰ (Appendix Table S5), suggest that oxidation of organic materials within the sediments contributed to the reduction of the Mn oxides during diagenesis, although these values are slightly affected by organic carbon possessing low values (−19 to −14‰; Appendix Table S5). The pore water during burial diagenesis, especially for the L2 samples, originated partly from hydrothermal fluids, which resulted in variable Ca/Mn and Ca/Mg ratios and Eu anomalies of the samples (Sec. 4.1).

The formation of rhodochrosite requires a reduced and alkaline environment (e.g., Mücke et al. 1999). If the transformation to rhodochrosite took place near the sediment-seawater interface where the geochemical system was open to seawater, then substantial amounts of Mn, together with Zn and Ni, could have been released and lost from the sediments. However, because the Nsuta deposit is extensively large and shows high Mn concentrations (Dixon 1979; Nyame 2008; Nyame et al. 2003), most of the Mn probably was not lost during the mineral transformation. Instead, rhodochrosite in the Nsuta deposit likely formed at burial depths where the geochemical system was less open. This view is supported by the enrichments of Zn and Ni in the rhodochrosite. It is also consistent with the finding from modern equatorial Pacific sediments of early-diagenetic rhodochrosite minerals at ~30 m depth below seafloor (Meister et al. 2009).

Our genetic model of the Nsuta deposit suggests that at the existed depositional environment, dissolved O_2 concentration was sufficiently high for the precipitation of MnO_2. Experimental data showed that Mn oxides can be precipitated under rather low-O_2 conditions (~0.2 μM) through microbial oxidation of dissolved Mn^{2+} (Clement et al. 2009). However, under such conditions, Mn oxides buried in sediments would be easily reduced and released into overlying seawater as dissolved Mn^{2+} (Scott and Lyons 2012; Shaw et al., 1990). In contrast, if the bottom water O_2 concentration is higher than 10 μM, Mn^{2+} in pore water can be reprecipitated as Mn oxides at/near the sediment–seawater interface (Scott and Lyons 2012; Shaw et al., 1990). This behavior of Mn suggests that dissolved O_2 concentration in the Nsuta depositional environment would have been higher than 10 μM.

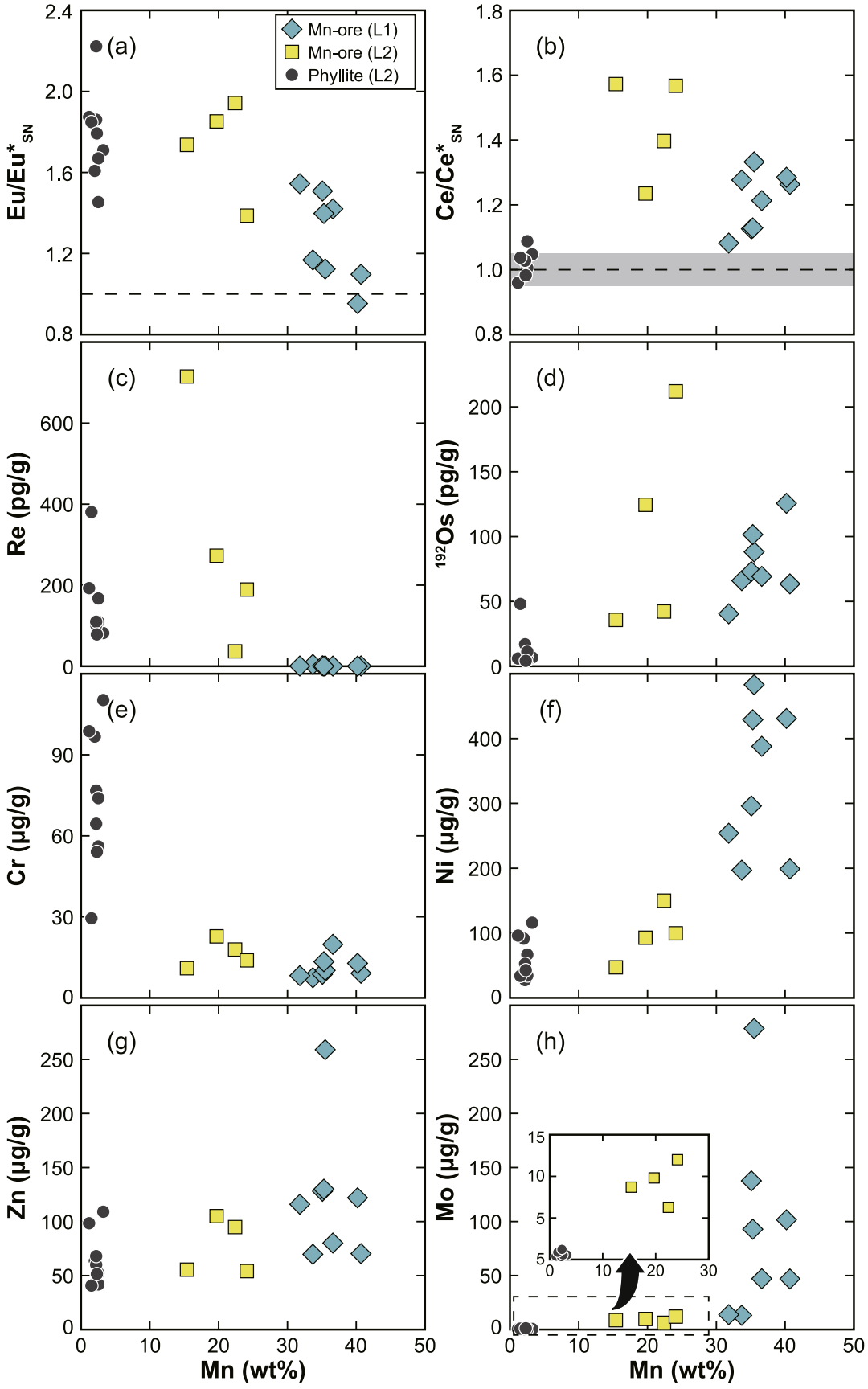

Fig. 4. Trace element contents of Mn-ore and phyllite samples taken from the Nsuta deposit. Magnitudes of the (a) Eu and (b) Ce anomalies in the PAAS-normalized REE patterns and concentrations of (c) Re, (d) Os, (e) Cr, (f) Ni, (g) Zn, and (h) Mo with respect to the Mn content.

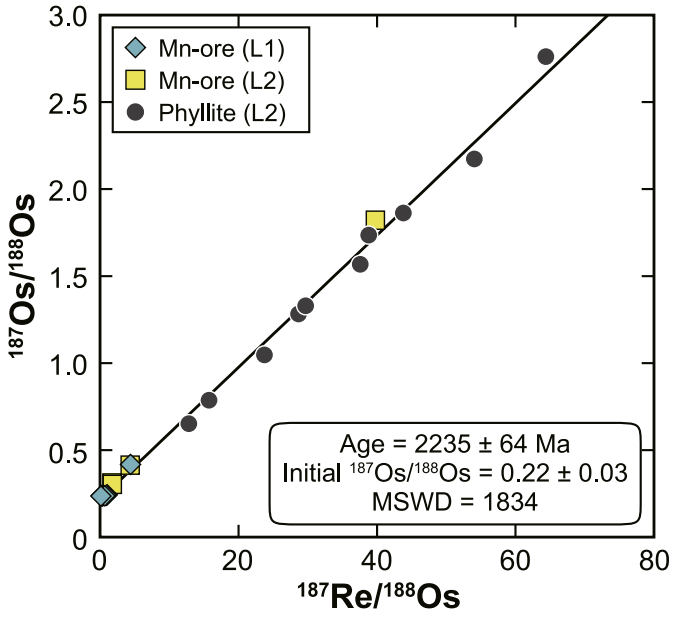

Fig. 5. Re-Os isochron diagram for Mn-ore and phyllite samples taken from the Nsuta deposit. The Re-Os data yield a Re-Os isochron age of 2235 ± 64 Ma with an initial $^{187}Os/^{188}Os$ of 0.22 ± 0.03 using *Isoplot 4.15* (Ludwig 2008).

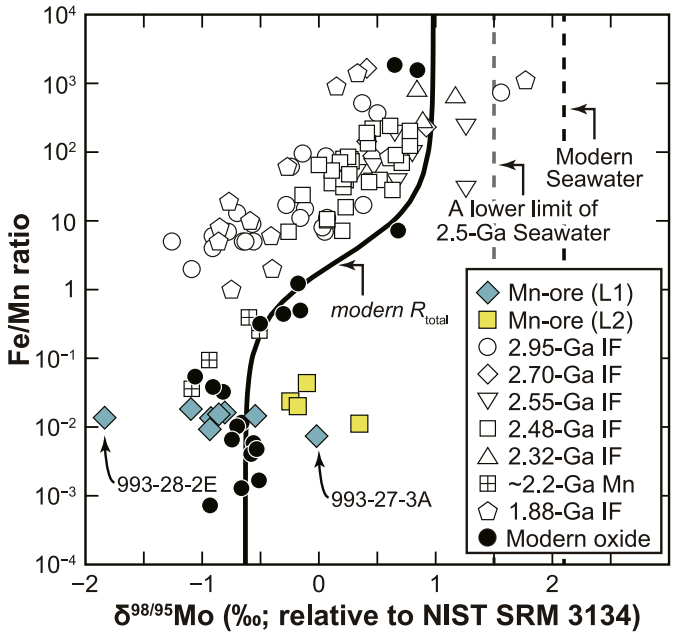

Fig. 6. $\delta^{98/95}$Mo–Fe/Mn diagram, modified from Goto et al. (2020), showing data of Mn-ore samples collected from the Nsuta deposit. The diagram originally included the $\delta^{98/95}$Mo values of modern marine oxides significantly affected by hydrothermal fluids. Here, *modern* R_{total} denotes the $\delta^{98/95}$Mo of modern marine Fe-Mn oxides calculated using both modern seawater $\delta^{98/95}$Mo values and the Mo isotopic fractionation factors due to the adsorption of Mo onto Fe and Mn oxides (Goto et al. 2020).

4.3. Mo isotopic compositions: Global redox conditions

Secular variations in seawater $\delta^{98/95}$Mo generally reflect changes in the global ocean redox conditions (e.g., Dahl et al., 2010; Siebert et al. 2003). We proposed previously that the $\delta^{98/95}$Mo values of Fe- and Mn-rich sedimentary rocks can be explained by Mo isotopic fractionation during adsorption onto Fe oxide and Mn oxides (Goto et al. 2020). The isotopic fractionation during the adsorption of Mo in modern seawater onto Fe and Mn oxides explains the measured $\delta^{98/95}$Mo values of modern hydrothermal Fe-Mn oxides (see solid curve of *modern* R_{total} in Fig. 6) (Goto et al. 2020). This means that the paleo-seawater $\delta^{98/95}$Mo at the time of sedimentation can be reconstructed based on the $\delta^{98/95}$Mo values of ancient Fe- and Mn-rich sedimentary rocks. Goto et al. (2020) reconstructed mid-Archean (~2.9 Ga) to late-Paleoproterozoic (~1.8 Ga) seawater $\delta^{98/95}$Mo values using the $\delta^{98/95}$Mo values of various Fe- and Mn-rich sediments measured by previous studies (Cabral et al. 2019; Canfield et al. 2013; Kurzweil et al. 2015, 2016; Planavsky et al. 2014, 2018; Ossa Ossa et al. 2018). The reconstructed values are generally consistent with records for euxinic shales (Duan et al. 2010; Kendall et al. 2011). However, data for ~2.2 Ga are still required to understand the global ocean redox conditions during the O_2 overshoot. Because the primary minerals of the Nsuta deposit were likely Mn oxides, Mn-ore samples collected from the deposit may provide information on the mid-Paleoproterozoic seawater $\delta^{98/95}$Mo at ~2.2 Ga. In this section, we first describe the $\delta^{98/95}$Mo data of Mn-ore samples from the Nsuta deposit (Sec. 4.3.1) and then discuss the global ocean redox conditions during the mid-Paleoproterozoic (Sec. 4.3.2). Although two methods were applied to digest the samples (Sec. 3.4), the values and/or trends discussed below did not change significantly (Appendix Table S4). To minimize the influence of Mo derived from detrital and/or organic materials, in the following discussion, we focus on the data obtained by HCl leaching.

4.3.1. $\delta^{98/95}$Mo of the Nsuta deposit

$\delta^{98/95}$Mo values of the Nsuta deposit are shown in Figs. 6 and 7. One sample (993–27–3A) is excluded from the following discussion because this sample shows a high TOC content (> 0.2 wt%) with a low Mo/TOC value (Fig. 7b). Organic material can be an efficient host for Mo in Fe- and Mn-rich sedimentary rocks (e.g., Kurzweil et al. 2015). Hence, the $\delta^{98/95}$Mo value of this sample may not represent the isotopic compositions of Mo hosted in the Mn-bearing minerals (Goto et al. 2020). All the Mn-ore samples from the Nsuta deposit have low Fe/Mn ratios ($< 10^{-1}$) (Fig. 6), which cannot be explained by Fe release during diagenesis (e.g., Shaw et al. 1990). This suggests that the samples are expected to have a uniform $\delta^{98/95}$Mo value determined primarily by isotopic fractionation during the adsorption of Mo onto Mn oxides (Goto et al. 2020). Measured $\delta^{98/95}$Mo values of the Mn-ore samples cluster around −1‰ to −0.5‰, although the $\delta^{98/95}$Mo values vary significantly between −1.84‰ and +0.35‰ (Fig. 6).

Given that the analyzed samples are predominantly composed of early diagenetic rhodochrosite, the early diagenesis could have caused variation in the $\delta^{98/95}$Mo values. Poulson-Brucker et al. (2009) reported a depth $\delta^{98/95}$Mo profile of modern Mn-rich hemipelagic sediments from the Guatemala Basin in the eastern Pacific (MANOP Site H). Although the pore-water data from the sediments indicated reductive dissolution of Mn oxides, the sediments showed a constant $\delta^{98/95}$Mo value through the sediment column. Therefore, we suggest that the formation of rhodochrosite from Mn oxides during early diagenesis probably did not alter the primary $\delta^{98/95}$Mo values significantly. In addition, high Mn contents of the Nsuta Mn-ore samples (Fig. 3) are inconsistent with the reductive dissolution of Mn oxides and subsequent Mn^{2+} release to seawater that would result in low-Mn contents (Poulson-Brucker et al., 2009).

Then, what might the causative mechanisms be for the variations in the $\delta^{98/95}$Mo values of the Nsuta Mn-ore samples shown in Fig. 6? First, we consider that Mo from hydrothermal fluids to the L2 samples would be affected by direct additions (i.e., without adsorption onto Mn oxides) of Mo from hydrothermal fluids. This is because our geochemical data (e.g., high Ca/Mg ratios; Fig. 3) strongly suggest that the L2 samples were affected by hydrothermal fluids during early diagenesis (Sec. 4.1). The L2 samples tend to have higher $\delta^{98/95}$Mo values (−0.3‰ to +0.4‰) than the clustered data of L1 samples (at around −1.0‰ to −0.5‰; Figs. 6 and 7). The $\delta^{98/95}$Mo values of L2 samples positively correlate

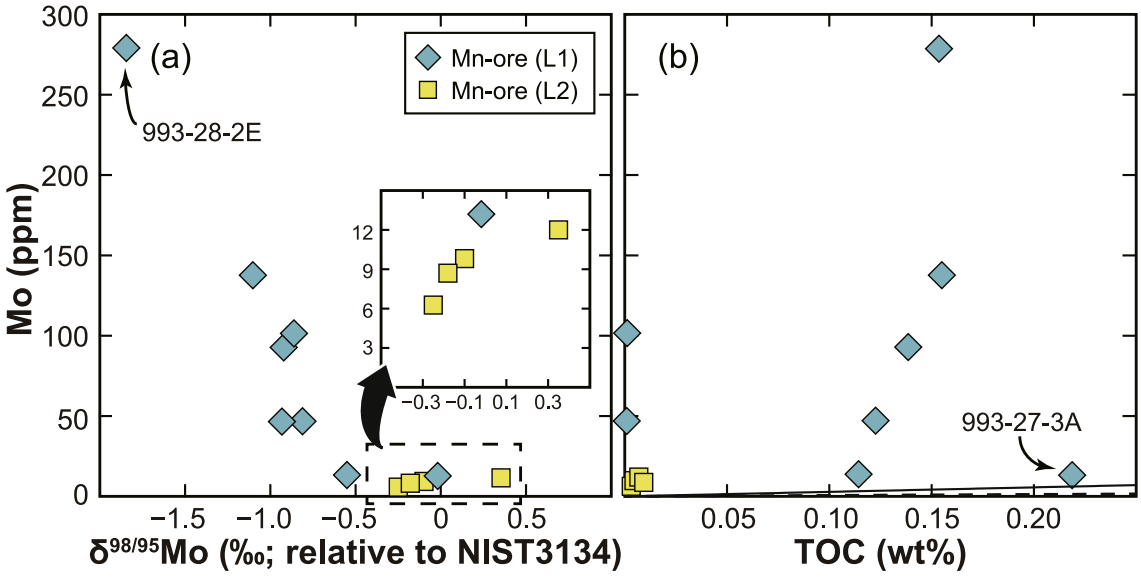

Fig. 7. Crossplots of Mo concentration versus (a) $\delta^{98/95}$Mo and (b) TOC content of Mn-ore samples collected from the Nsuta deposit. The dashed and solid lines in (b) show Mo/TOC ratios of Proterozoic (6 μg/g /wt%) and Phanerozoic (28 μg/g /wt%) black shales, respectively (Scott et al. 2008). The low $\delta^{98/95}$Mo value of sample 993–28–2E may reflect Mo adsorption from hydrothermal fluids onto Mn oxides. The high $\delta^{98/95}$Mo value of sample 993–27–3A may indicate significant incorporation of Mo adsorbed onto organic material.

with Mo concentrations (Fig. 7a), suggesting additions of isotopically heavy Mo into the sediments. The highest $\delta^{98/95}$Mo value of +0.4‰ among the L2 samples is close to that of hydrothermal fluids reported from a modern hydrothermal system in the Juan de Fuca Ridge ($\delta^{98/95}$Mo = ~+0.6‰; McManus et al. 2002). Hence, the high $\delta^{98/95}$Mo values in the L2 samples can be attributed to the enrichment of isotopically heavy Mo from the pore water affected by hydrothermal fluids. Because Mn oxides preferentially adsorb isotopically light Mo with a fractionation factor of ~−2.7‰ (Wasylenki et al. 2008), the isotopically heavy Mo in the L2 samples was probably not acquired through adsorption onto Mn oxides but would have been directly incorporated into rhodochrosite during/after its formation. In contrast, there is no positive correlation between the Mo contents and $\delta^{98/95}$Mo values of the L1 samples, although some samples with high Mo concentrations show low $\delta^{98/95}$Mo values (Fig. 7a). Given the seawater-like Ca/Mg ratios of the L1 samples, Mo originated from hydrothermal fluids might have had little effect on their $\delta^{98/95}$Mo values during/after mineral transformation (Fig. 3a; Sec. 4.1).

The $\delta^{98/95}$Mo values of samples from L1 exhibit less scatter with a mean value of −1.00 ± 0.40‰, 1SD. However, there is still a variation between −1.84‰ and −0.55‰ that needs explanation (Figs. 6 and 7), although this range is similar to that of the $\delta^{98/95}$Mo values of ~2.0-Ga Mn-ore samples from Morro da Mina (from −1.80‰ to −0.47‰; Cabral et al. 2019). The variation appears mainly due to the lowest $\delta^{98/95}$Mo value of sample 993–28–2E (−1.84‰), which is significantly lower than the other $\delta^{98/95}$Mo data of L1 samples (Figs. 6 and 7). The lowest $\delta^{98/95}$Mo value of sample 993–28–2E is close to those of hydrothermal Mn oxides collected from the modern Samoan hotspot (Goto et al. 2020). The low values of the modern Samoan hotspot were interpreted to reflect the contribution of isotopic fractionation during the adsorption of hydrothermally derived Mo. This is because hydrothermally derived Mo possesses lower $\delta^{98/95}$Mo values (e.g., ~+0.6‰; McManus et al. 2002) than ambient seawater. If Mo with a $\delta^{98/95}$Mo of +0.6‰ adsorbed from hydrothermal fluids onto Mn oxides, that Mo in Mn oxides could exhibit a $\delta^{98/95}$Mo of ~−2.1‰ due to the large isotopic fractionation (~−2.7‰) during the adsorption process. Sample 993–28–2E is characterized by a high Mo content (i.e., 279 μg/g) compared with the other Mn-ore samples (Fig. 7). This sample also shows the highest Ni and Zn concentrations (483 and 259 μg/g, respectively) among the samples; Mo, Ni, and Zn are among the few metals known to be enriched in hydrothermal Mn-oxide deposits in the modern ocean basins (Hein et al. 1997). Hence, sample 993–28–2E may have acquired metals from hydrothermal fluids in addition to ambient seawater before the conversion of Mn-oxide to rhodochrosite. If sample 993–28–2E is excluded from L1, the $\delta^{98/95}$Mo range would narrow, ranging from −1.10 to −0.55‰ with a mean value of −0.86 ± 0.18‰, 1SD. Based on petrographic and geochemical data, we suggest that the $\delta^{98/95}$Mo values of −0.86 ± 0.18‰ are representative of the least altered Mn-ore samples in the Nsuta deposit. Because Mn oxides were likely the primary precipitates in the Nsuta deposit (Sec. 4.2), the observed values can be attributed to isotopic fractionation during adsorption of contemporary seawater Mo onto Mn oxides.

4.3.2. *$\delta^{98/95}$Mo of mid-Paleoproterozoic seawater*

Using the $\delta^{98/95}$Mo values of the least altered samples and the mass-balance calculation of Mo isotopic fractionation (Goto et al. 2020), we can estimate the seawater $\delta^{98/95}$Mo values at the time of deposition of the Nsuta deposit (~2.2 Ga). The previous study showed a possible positive excursion in the reconstructed seawater $\delta^{98/95}$Mo record during the mid-Paleoproterozoic; namely, the $\delta^{98/95}$Mo values increased from +1.5‰ to +2.1‰ at 2.35 Ga, remained stable at ~+1.9–2.1‰ between 2.35 and 2.2 Ga, and then decreased to ~+1.2‰ by 1.88 Ga (Fig. 8a; Goto et al. 2020). Some of the samples from ~2.0-Ga Mn-ore from Morro da Mina in Brazil also suggest high seawater $\delta^{98/95}$Mo during the mid-Paleoproterozoic; however, the calculated values also show a large variation (i.e., mean $\delta^{98/95}$Mo = 1.65 ± 0.41‰, 1SD) that could be caused by the influence of Mo associated with organic material and/or metamorphic alteration. Based on the mas-balance calculation that considers the isotopic fractionation during adsorption onto oxides (Goto et al. 2020), the obtained $\delta^{98/95}$Mo values of the least altered samples from the Nsuta deposit suggest a seawater $\delta^{98/95}$Mo of +1.85 ± 0.18‰ at ~2.2 Ga, confirming the existence of an isotopically heavy reservoir of dissolved Mo in the oceans during the mid-Paleoproterozoic (Fig. 8a).

The Mo isotopic composition of seawater generally reflects the relative proportions of Mo removal into strongly euxinic (i.e., [H_2S] > ~100 μM) (f_{eux}), reducing (i.e., [H_2S] < ~100 μM) (f_{red}), and oxic (f_{ox}) sinks (e.g., Dahl et al. 2010; Siebert et al. 2003). Assuming that the riverine Mo input is balanced by the outputs into euxinic, reducing, and oxic sediments, seawater $\delta^{98/95}$Mo (R_{sw}) can be estimated using the

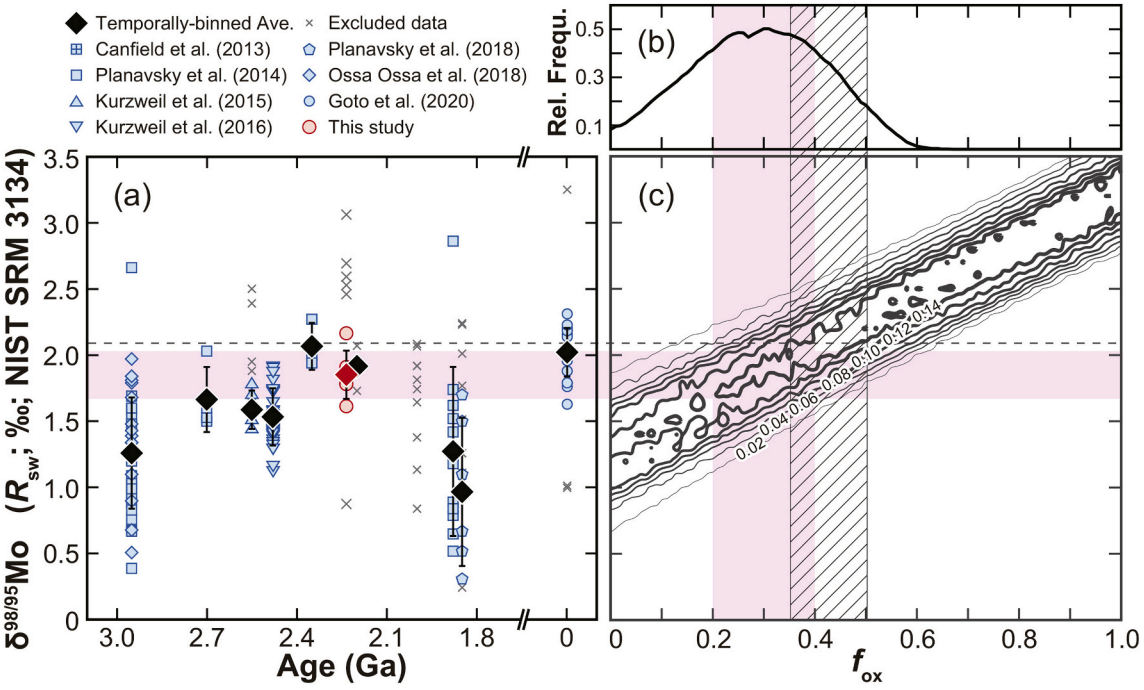

Fig. 8. (a) Secular variations in seawater $\delta^{98/95}$Mo reconstructed from Fe- and Mn-rich sedimentary rocks, as modified from Goto et al. (2020), and the results of Monte Carlo calculation showing (b) the relative frequency of calculated seawater $\delta^{98/95}$Mo (R_{sw} in Eq. (1)) compatible with mid-Paleoproterozoic seawater $\delta^{98/95}$Mo (+1.85 ± 0.18‰) inferred from the Nsuta deposit and (c) R_{sw} as a function of the relative size of the oxic sink (f_{ox}) (see Eq. (1) in the text). The $\delta^{98/95}$Mo in (a) are calculated using a mass-balance model and are reported relative to NIST 3134 (Goto et al. 2020). The data for the Nsuta deposit are highlighted in red in panel (a). The ranges of mid-Paleoproterozoic seawater $\delta^{98/95}$Mo inferred from the Nsuta samples and f_{ox} (~0.2–0.4) that are particularly consistent with the inferred $\delta^{98/95}$Mo (or R_{sw}) are shaded as red in panels (a) and (c). The grey crosses in panel (a) show samples with high TOC or affected by hydrothermal fluids (Sec. 4.3.1; Goto et al. 2020), which were disregarded in the calculations of the mean $\delta^{98/95}$Mo values. The dashed line in panels (a) and (c) indicates modern seawater values ($\delta^{98/95}$Mo = +2.09‰; Nakagawa et al. 2012; Siebert et al. 2003). The hatched area in panels (b) and (c) shows the range of modern f_{ox} (~0.35–0.50; Poulson-Brucker et al., 2009; Scott et al. 2008;). The contours in panel (c) show the range of the relative frequency of R_{sw} for each f_{ox}. (For interpretation of the references to colour in this figure legend, the reader is referred to the web version of this article.)

following equation:

$$R_{sw} = R_{riv} - (f_{eux}\Delta_{eux} + f_{red}\Delta_{red} + f_{ox}\Delta_{ox}) \quad (1)$$

where R_{riv} denotes the riverine $\delta^{98/95}$Mo, and Δ_{eux}, Δ_{red}, and Δ_{ox} respectively denote the isotopic fractionation factors of Mo removal into euxinic, reducing, and oxic sediments from seawater. Euxinic sediments effectively remove Mo and cause small isotopic fractionation (i.e., Δ_{eux} = −0.48 ± 0.29‰, 1SD; Nägler et al. 2011; Noordmann et al. 2015; Appendix Table S6), although sediments deposited under highly euxinic conditions often possess $\delta^{98/95}$Mo values that are comparable to the contemporary seawater value (e.g., Romaniello et al. 2016). Reducing sediments show lower (more negative) Δ_{red} values than Δ_{eux} (i.e., Δ_{red} = −1.05 ± 0.35‰, 1SD; Poulson et al. 2006; Poulson-Brucker et al., 2009; Siebert et al. 2006; Appendix Table S7). Oxic sediments cause the largest isotopic fractionation among the sinks (i.e., −2.72 ± 0.17‰, 1SD; Wasylenki et al. 2008; Appendix Table S8). This is partly because we assume that Mo is removed through adsorption onto Mn oxides in oxic sediments, although dissolved Mo can be also removed via adsorption onto Fe oxides (Goldberg et al. 2009). As for the riverine $\delta^{98/95}$Mo, we use a weighted mean $\delta^{98/95}$Mo value of the modern riverine (0.51 ± 0.33‰, 1SD; Archer and Vance 2008; Appendix Table S9), which is slightly higher than an average value for the upper continental crust (~+0.15‰; Willbold and Elliot, 2017). Using Eq. (1), R_{sw} was calculated as a function of f_{ox} that varied from 0 to 1. Because of the large uncertainties for the parameters used in Eq. (1), the Monte Carlo simulation method was employed to evaluate a possible range of R_{sw}. The calculations were conducted 1000 times for each f_{ox}. The other parameters (f_{eux}, f_{red}, R_{riv}, Δ_{eux}, Δ_{red}, and Δ_{ox}) were randomly sampled from their reasonable ranges. The ranges of R_{riv}, Δ_{eux}, Δ_{red}, and Δ_{ox} were determined from one-standard-deviations of the previously reported data (Appendix Tables S6–S9).

The results of the calculation are shown as the relative frequency of each R_{sw} (= $\delta^{98/95}$Mo of seawater) in Figs. 8b and c. As f_{ox} increases, R_{sw} increases linearly because isotopically light Mo is effectively removed to oxic sediments (Fig. 8c). Fig. 8c also shows that a spread of the allowable R_{sw} range becomes wide at low f_{ox} values, compared to those at high f_{ox} values. The wide spread can be attributed to the uncertainties inherent in Δ_{eux} and Δ_{red} (0.29‰ and 0.35‰, respectively). These uncertainties have a limited effect on the calculated R_{sw} for high f_{ox}.

The results of the calculations are generally consistent with modern seawater conditions (Fig. 8c). The modern seawater $\delta^{98/95}$Mo value of +2.09‰ (Nakagawa et al. 2012; Siebert et al. 2003) can be found in the high frequency area (> 0.14) for the calculations using f_{ox} = ~0.35–0.50 (Poulson-Brucker et al., 2009; Scott et al. 2008). This observation may indicate that the high-frequency area (> 0.14) represents the realistic ocean conditions. The R_{sw} values of +1.85 ± 0.18‰ that are compatible with the measured $\delta^{98/95}$Mo of the 2.2-Ga Nsuta deposit can be reproduced for a wide range of f_{ox} (i.e., f_{ox} = ~0–0.6; Fig. 8b) given the uncertainties of the parameters in Eq. (1). Nevertheless, considerably high relative frequency (> 0.4) of those R_{sw} values occurs in the calculations using f_{ox} = ~0.2–0.4 (Fig. 8b). This peak of relative frequency would shift to higher f_{ox} if we include Mo removal via Fe oxides. This is because the isotopic fractionation factors during Mo adsorption onto Fe oxides, ranging from −2.2‰ to −0.8‰ (Goldberg et al. 2009), are less negative than that exhibited by Mo adsorption onto Mn oxides (−2.72 ± 0.17‰, 1SD; Wasylenki et al. 2008). Thus, f_{ox} would be greater than ~0.2–0.4 when considering the occurrence of Fe oxides.

Figs. 8b and c indicate that the positive $\delta^{98/95}$Mo (or R_{sw}) excursion from ~1.1–1.6‰ in the Late Archean to ~1.8–2.1‰ in the mid-

Paleoproterozoic (Fig. 8a) can be explained by an increase in the fraction of Mo removal into the oxic sink (f_{ox}). These figures also suggest that the R_{sw} change is possible without increasing f_{ox}. As expected from Eq. (1), shifts of Δ_{eux} and/or Δ_{red} to more negative values and/or increases in f_{red} and/or R_{riv} may also elevate R_{sw}. However, Δ_{eux} and Δ_{red} probably would not change over geological time, although these values could be variable depending on locations due to local redox conditions (e.g., Poulson et al. 2006; Poulson-Brucker et al., 2009). In addition, to achieve high $\delta^{98/95}$Mo values (> 1.8‰) under low f_{ox} conditions ($f_{ox} < 0.1$), considerably high f_{red} values are required ($f_{red} > \sim 0.7–0.9$). In contrast, a positive shift in R_{riv} probably requires high f_{ox} conditions. This is because high R_{riv} would be caused by isotopic fractionation associated with Mo removal via oxides or organic material during the transport of Mo from continental crust to seawater (Archer and Vance 2008; King and Pett-Ridge 2018), although the extent of terrestrial life during the mid-Paleoproterozoic was probably small. It is more likely that the high $\delta^{98/95}$Mo values during the mid-Paleoproterozoic represent an increase in the oxic Mo sink during that period, given the high frequency of R_{sw} values of $+1.85 \pm 0.18$‰ in the calculations using $f_{ox} = \sim 0.2–0.4$. Thus, the reconstructed mid-Paleoproterozoic seawater $\delta^{98/95}$Mo value suggests that the precipitation of Nsuta primary Mn oxides was not a spatially restricted phenomenon in the mid-Paleoproterozoic oceans and should have been widespread. This view is consistent with the occurrence of multiple large Mn deposits in volcano-sedimentary successions during this time period (Johnson et al. 2016; Maynard, 2010). Because Mn oxides effectively scavenge dissolve elements, extensive deposition of the oxides may have significantly influenced the distribution of dissolved trace elements in mid-Paleoproterozoic seawater. This possibility could be further examined to ascertain the existence of a relationship between biogenic and environmental evolution, the so-called bio-inorganic bridge (Anbar and Knoll 2002). In contrast, no significant fraction ($f_{ox} = 0$) of the oxic sink is required to explain the low R_{sw} values of ~1.1‰ at ~2.9 Ga and ~ 1.9 Ga. This is consistent with the limited occurrence of Mn-rich deposits during the Archean and Mesoproterozoic (Johnson et al. 2016; Maynard 2010).

As discussed in Sec. 4.2, Mn oxides can be precipitated and preserved in sediments only if the bottom seawater O_2 levels are higher than 10 μM (Scott and Lyons 2012; Shaw et al., 1990). Given the reconstructed high seawater $\delta^{98/95}$Mo value, the bottom water containing dissolved O_2 concentrations of > 10 μM would have expanded during the mid-Paleoproterozoic, although the $\delta^{98/95}$Mo data cannot constrain whether the oxidizing conditions (or the deposition of Mn oxides) were restricted in continental margins or also prevailed in abyssal plains. Our lower limit of seawater O_2 levels existed at that time is consistent with but provides a more restricted value than those provided by previous studies (> 0.4–1 μM; Hardisty et al. 2014; Kipp et al. 2017). Hardisty et al. (2014) measured high I/(Ca + Mg) ratios in carbonate rocks deposited ~2.5–2.1 Gyr ago. The high I/(Ca + Mg) ratios reflect effective iodate (IO_3^-) formation in the oceans under oxidizing conditions with dissolved $O_2 > 1$ μM (Hardisty et al. 2014). Kipp et al. (2017) reported high $\delta^{82/78}$Se values for offshore shales deposited ~2.3–2.1 Gyr ago. They suggested that the high seawater $\delta^{82/78}$Se was caused by preferential reduction of isotopically light Se in shallow-marine environments (Kipp et al. 2017). Because partial reduction of Se occurs in the modern oceans with low dissolved O_2 levels (< 0.4 μM), a conservative lower limit of 0.4 μM was set for the dissolved O_2 concentration in shallow-marine environments. As noted by Kipp et al. (2017), the formation of IO_3^- and partial reduction of Se also occur in seawater with O_2 concentrations above 10 μM. Our estimate of seawater O_2 concentration in the mid-Paleoproterozoic can thus be reconciled with I/(Ca + Mg) and $\delta^{82/78}$Se records at ~2.3–2.1 Ga. The estimate is equivalent to > ~4–7% of the O_2 levels in modern open oceans. These values are sufficiently high for the survival of multicellular eukaryotes (Runnegar 1991; Waldbauer et al. 2011), and may have facilitated the first appearance of stem group eukaryotes in the geological records at ~2.2 Ga (El Albani et al. 2010, 2014; Sawaki et al. 2017).

5. Summary and conclusions

We provide data on the microstructures, major and trace element concentrations, and Re-Os and Mo isotopic compositions of Mn-carbonate ore and phyllite samples taken from two outcrops at the Nsuta deposit in the Birimian Supergroup, Ghana. The Mn-ore samples are predominantly composed of early diagenetic rhodochrosite. However, enrichments of Mo, Ni, Zn, and Os in the Mn-ore samples compared with those of the phyllite suggest a Mn-oxide precursor of the rhodochrosite that precipitated on the seafloor ~2.2 Gyr ago. This interpretation is supported by positive Ce anomalies found in the Mn-carbonate ore samples, but not the phyllite. Although some of the samples (e.g., samples from L2) were likely affected by hydrothermal fluids during early diagenesis, $\delta^{98/95}$Mo values (between −1.10‰ and − 0.55‰) of the least altered ore samples (e.g., the samples from L1) suggest a seawater $\delta^{98/95}$Mo of $+1.85 \pm 0.18$‰ at ~2.2 Ga. The reconstructed seawater $\delta^{98/95}$Mo value is higher than values for Archean and late Paleoproterozoic seawater inferred from black shales and IFs (Duan et al. 2010; Goto et al. 2020; Kendall et al. 2011). The high seawater $\delta^{98/95}$Mo during the mid-Paleoproterozoic can be best explained by the extensive deposition of Mn oxides under oxidizing marine conditions characterized by bottom seawater O_2 levels > 10 μM. Our $\delta^{98/95}$Mo results support the new view of O_2 overshoot during the mid-Paleoproterozoic, and seem to be consistent with the emergence of stem group eukaryotes at ~2.2 Ga.

Declaration of Competing Interest

The authors declare that they have no known competing financial interests or personal relationships that could have appeared to influence the work reported in this paper.

Acknowledgements

K. T. G. appreciates Mariah Mikesell for assistance with the sample preparation and J. R. H. thanks BHP Billiton for field support in Takoradi, Ghana and at the Nsuta mine. Eva Stüeken, Alexandre Raphael Cabral, and an anonymous reviewer are thanked for their constructive feedback. This study was a part of "Scientific Research on Genesis of Marine Resources," a project of Next-generation Technology for Ocean Resources Exploration of the Cross-ministerial Strategic Innovation Promotion Program (SIP). This study was also supported by JSPS KAKENHI (Grant No. JP15H02142, 26257211, and JP19K14832) and MEXT KAKENHI (Grant No. JP17H06456).

Appendix A. Supplementary data

Supplementary data to this article can be found online at https://doi.org/10.1016/j.chemgeo.2021.120116.

References

Anbar, A.D., Knoll, A.H., 2002. Proterozoic Ocean chemistry and evolution: a bioinorganic bridge? Science 297 (5584), 1137–1142. https://doi.org/10.1126/science.1069651.

Archer, C., Vance, D., 2008. The isotopic signature of the global riverine molybdenum flux and anoxia in the ancient oceans. Nat. Geosci. 1 (9), 597–600. https://doi.org/10.1038/ngeo282.

Atkins, A.L., Shaw, S., Peacock, C.L., 2014. Nucleation and growth of todorokite from birnessite: Implications for trace-metal cycling in marine sediments. Geochim. Cosmochim. Acta 144, 109–125. https://doi.org/10.1016/j.gca.2014.08.014.

Barrett, T.J., Taylor, P.N., Lugoqski, J., 1987. Metalliferous sediments from DSDP Leg 92: the East Pacific rise transect. Geochim. Cosmochim. Acta 51 (9), 2241–2253. https://doi.org/10.1016/0016-7037(87)90278-X.

Bau, M., 1991. Rare-earth element mobility during hydrothermal and metamorphic fluid-rock interaction and the significance of the oxidation state of europium. Chem. Geol. 93 (3–4), 219–230. https://doi.org/10.1016/0009-2541(91)90115-8.

Bau, M., Schmidt, K., Koschinsky, A., Hein, J., Kuhn, T., Usui, A., 2014. Discriminating between different genetic types of marine ferro-manganese crusts and nodules based

on rare earth elements and yttrium. Chem. Geol. 381, 1–9. https://doi.org/10.1016/j.chemgeo.2014.05.004.
Bekker, A., Holland, H.D., 2012. Oxygen overshoot and recovery during the early Paleoproterozoic. Earth Planet. Sci. Lett. 317, 295–304. https://doi.org/10.1016/j.epsl.2011.12.012.
Birck, J.L., Barman, M.R., Capmas, F., 1997. Re–Os isotopic measurements at the femtomole level in natural samples. Geostand. Newslett. 21 (1), 19–27. https://doi.org/10.1111/j.1751-908X.1997.tb00528.x.
Böttcher, M.E., 1998. Manganese (II) partitioning during experimental precipitation of rhodochrosite–calcite solid solutions from aqueous solutions. Mar. Chem. 62 (3–4), 287–297. https://doi.org/10.1016/S0304-4203(98)00039-5.
Cabral, A.R., Zeh, A., Vianna, N.C., Ackerman, L., Pašava, J., Lehmann, B., Chrastný, V., 2019. Molybdenum-isotope signals and cerium anomalies in Palaeoproterozoic manganese ore survive high-grade metamorphism. Sci. Rep. 9 (1), 4570. https://doi.org/10.1038/s41598-019-40998-5.
Canfield, D.E., Ngombi-Pemba, L., Hammarlund, E.U., Bengtson, S., Chaussidon, M., Gauthier-Lafaye, F., Meunier, A., Riboulleau, A., Rollion-Bard, C., Rouxel, O., Asael, D., Pierson-Wickmann, A.-C., El Albani, A., 2013. Oxygen dynamics in the aftermath of the Great Oxidation of Earth's atmosphere. Proc. Natl. Acad. Sci. U. S. A. 110 (42), 16736–16741. https://doi.org/10.1073/pnas.1315570110.
Chisonga, B.C., Gutzmer, J., Beukes, N.J., Huizenga, J.M., 2012. Nature and origin of the protolith succession to the Paleoproterozoic Serra do Navio manganese deposit, Amapa Province, Brazil. Ore Geol. Rev. 47, 59–76. https://doi.org/10.1016/j.oregeorev.2011.06.006.
Chow, N., Morad, S., Al-Aasm, I.S., 2000. Origin of authigenic Mn-Fe carbonates and pore-water evolution in marine sediments: evidence from Cenozoic strata of the Arctic Ocean and Norwegian-Greenland Sea (ODP Leg 151). J. Sediment. Res. 70 (3), 682–699. https://doi.org/10.1306/2DC40930-0E47-11D7-8643000102C1865D.
Clement, B.G., Luther III, G.W., Tebo, B.M., 2009. Rapid, oxygen-dependent microbial Mn (II) oxidation kinetics at sub-micromolar oxygen concentrations in the Black Sea suboxic zone. Geochim. Cosmochim. Acta 73 (7), 1878–1889. https://doi.org/10.1016/j.gca.2008.12.023.
Coggon, R.M., Teagle, D.A., Smith-Duque, C.E., Alt, J.C., Cooper, M.J., 2010. Reconstructing past seawater Mg/Ca and Sr/Ca from mid-ocean ridge flank calcium carbonate veins. Science 327 (5969), 1114–1117. https://doi.org/10.1126/science.1182252.
Cohen, A.S., Waters, F.G., 1996. Separation of osmium from geological materials by solvent extraction for analysis by thermal ionisation mass spectrometry. Anal. Chim. Acta 332 (2–3), 269–275. https://doi.org/10.1016/0003-2670(96)00226-7.
Coogan, L.A., Gillis, K.M., 2018. Low-temperature alteration of the seafloor: impacts on ocean chemistry. Annu. Rev. Earth Planet. Sci. 46, 21–45. https://doi.org/10.1346/CCMN.2012.0600607.
Dahl, T.W., Hammarlund, E.U., Anbar, A.D., Bond, D.P., Gill, B.C., Gordon, G.W., Knoll, A.H., Nielsen, A.T., Schovsbo, N.H., Canfield, D.E., 2010. Devonian rise in atmospheric oxygen correlated to the radiations of terrestrial plants and large predatory fish. Proc. Natl. Acad. Sci. U. S. A. 107 (42), 17911–17915. https://doi.org/10.1073/pnas.1011287107.
Dixon, C.J., 1979. The Nsuta Manganese Deposit-Ghana. In: Dixon, C.J. (Ed.), Atlas of Economic Mineral Deposits. Springer, Netherlands, pp. 20–21.
Duan, Y., Anbar, A.D., Arnold, G.L., Lyons, T.W., Gordon, G.W., Kendall, B., 2010. Molybdenum isotope evidence for mild environmental oxygenation before the Great Oxidation Event. Geochim. Cosmochim. Acta 74 (23), 6655–6668. https://doi.org/10.1016/j.gca.2010.08.035.
El Albani, A., Bengtson, S., Canfield, D.E., Bekker, A., Macchiarelli, R., Mazurier, A., Hammarlund, E.U., Boulvais, P., Dupuy, J.-J., Fontaine, C., Fürsich, F.T., Gauthier-Lafaye, F., Janvier, P., Javaux, E., Ossa Ossa, F., Pierson-Wickmann, A.-C., Riboulleau, A., Sardini, P., Vachard, D., Whitehouse, M., Meunier, A., 2010. Large colonial organisms with coordinated growth in oxygenated environments 2.1 Gyr ago. Nature 466 (7302), 100–104. https://doi.org/10.1038/nature09166.
El Albani, A., Bengtson, S., Canfield, D.E., Riboulleau, A., Bard, C.R., Macchiarelli, R., Pemba, L.N., Hammarlund, E., Meunier, A., Mouele, I.M., Benzerara, K., Bernard, S., Boulvais, P., Chaussidon, M., Cesari, C., Fontaine, C., Chi-Fru, E., Ruiz, J.M.G., Gauthier-Lafaye, F., Mazurier, A., Pierson-Wickmann, A.-C., Rouxel, O., Trentesaux, A., Vecoli, M., Versteegh, G.J.M., White, L., Whitehouse, M., Bekker, A., 2014. The 2.1 Ga old Francevillian biota: biogenicity, taphonomy and biodiversity. PLoS One 9 (6), e99438. https://doi.org/10.1371/journal.pone.0099438.
Goldberg, T., Archer, C., Vance, D., Poulton, S.W., 2009. Mo isotope fractionation during adsorption to Fe (oxyhydr) oxides. Geochim. Cosmochim. Acta 73 (21), 6502–6516. https://doi.org/10.1016/j.gca.2009.08.004.
Gordon, G.W., Lyons, T.W., Arnold, G.L., Roe, J., Sageman, B.B., Anbar, A.D., 2009. When do black shales tell molybdenum isotope tales? Geology 37 (6), 535–538. https://doi.org/10.1130/G25186A.1.
Goto, K.T., Sekine, Y., Shimoda, G., Hein, J.R., Aoki, S., Ishikawa, A., Suzuki, K., Gordon, G.W., Anbar, A.D., 2020. A framework for understanding Mo isotope records of Archean and Paleoproterozoic Fe- and Mn-rich sedimentary rocks: Insights from modern marine hydrothermal Fe-Mn oxides. Geochim. Cosmochim. Acta 280, 221–236. https://doi.org/10.1016/j.gca.2020.04.017.
Grenholm, M., Jessell, M., Thébaud, N., 2019. A geodynamic model for the Paleoproterozoic (ca. 2.27–1.96 Ga) Birimian Orogen of the southern West African Craton–Insights into an evolving accretionary-collisional orogenic system. Earth Sci. Rev. 192, 138–193. https://doi.org/10.1016/j.earscirev.2019.02.006.
Harada, M., Tajika, E., Sekine, Y., 2015. Transition to an oxygen-rich atmosphere with an extensive overshoot triggered by the Paleoproterozoic snowball. Earth Planet. Sci. Lett. 419, 178–186. https://doi.org/10.1016/j.epsl.2015.03.005.
Hardisty, D.S., Lu, Z., Planavsky, N.J., Bekker, A., Philippot, P., Zhou, X., Lyons, T.W., 2014. An iodine record of Paleoproterozoic surface ocean oxygenation. Geology 42 (7), 619–622. https://doi.org/10.1130/G35439.1.
Hein, J.R., Koschinsky, A., Halbach, P., Manheim, F.T., Bau, M., Kang, J.-K., Lubick, N., 1997. Iron and Manganese oxide Mineralization in the Pacific. Geological Society of London Special Publication No. 119, London, pp. 123–138.
Hein, J.R., Fan, D., Ye, J., Liu, T., Yeh, H.-W., 1999. Composition and origin of early Cambrian Tiantaishan phosphorite-Mn carbonate ores, Shaanxi Province, China. Ore Geol. Rev. 15 (1–3), 95–134. https://doi.org/10.1016/S0169-1368(99)00017-7.
Holland, H.D., 2006. The oxygenation of the atmosphere and oceans. Philos. Trans. R. Soc. London, Ser. B 361 (1470), 903–915. https://doi.org/10.1098/rstb.2006.1838.
Johnson, J.E., Webb, S.M., Ma, C., Fischer, W.W., 2016. Manganese mineralogy and diagenesis in the sedimentary rock record. Geochim. Cosmochim. Acta 173, 210–231. https://doi.org/10.1016/j.gca.2015.10.027.
Karhu, J.A., Holland, H.D., 1996. Carbon isotopes and the rise of atmospheric oxygen. Geology 24 (10), 867–870. https://doi.org/10.1130/0091-7613(1996)024<0867:CIATRO>2.3.CO;2.
Kato, Y., Fujinaga, K., Suzuki, K., 2005. Major and trace element geochemistry and Os isotopic composition of metalliferous umbers from the late cretaceous Japanese accretionary complex. Geochem. Geophys. Geosyst. 6 (7), Q07004 https://doi.org/10.1029/2005GC000920.
Kendall, B., Gordon, G.W., Poulton, S.W., Anbar, A.D., 2011. Molybdenum isotope constraints on the extent of late Paleoproterozoic Ocean euxinia. Earth Planet. Sci. Lett. 307 (3–4), 450–460. https://doi.org/10.1016/j.epsl.2011.05.019.
King, E.K., Pett-Ridge, J.C., 2018. Reassessing the dissolved molybdenum isotopic composition of ocean inputs: the effect of chemical weathering and groundwater. Geology 46 (11), 955–958. https://doi.org/10.1130/G45124.1.
Kipp, M.A., Stüeken, E.E., Bekker, A., Buick, R., 2017. Selenium isotopes record extensive marine suboxia during the Great Oxidation Event. Proc. Natl. Acad. Sci. U. S. A. 114 (5), 875–880. https://doi.org/10.1073/pnas.1615867114.
Kirschvink, J.L., Gaidos, E.J., Bertani, L.E., Beukes, N.J., Gutzmer, J., Maepa, L.N., Steinberger, R.E., 2000. Paleoproterozoic snowball Earth: Extreme climatic and geochemical global change and its biological consequences. Proc. Natl. Acad. Sci. U. S. A. 97 (4), 1400–1405. https://doi.org/10.1073/pnas.97.4.1400.
Kuhn, T., Bau, M., Blum, N., Halbach, P., 1998. Origin of negative Ce anomalies in mixed hydrothermal–hydrogenetic Fe–Mn crusts from the Central Indian Ridge. Earth Planet. Sci. Lett. 163 (1–4), 207–220. https://doi.org/10.1016/S0012-821X(98)00188-5.
Kurzweil, F., Wille, M., Schoenberg, R., Taubald, H., Van Kranendonk, M.J., 2015. Continuously increasing δ^{98}Mo values in Neoarchean black shales and iron formations from the Hamersley Basin. Geochim. Cosmochim. Acta 164, 523–542. https://doi.org/10.1016/j.gca.2015.05.009.
Kurzweil, F., Wille, M., Gantert, N., Beukes, N.J., Schoenberg, R., 2016. Manganese oxide shuttling in pre-GOE oceans–evidence from molybdenum and iron isotopes. Earth Planet. Sci. Lett. 452, 69–78. https://doi.org/10.1016/j.epsl.2016.07.013.
Large, R.R., Halpin, J.A., Danyushevsky, L.V., Maslennikov, V.V., Bull, S.W., Long, J.A., Gregory, D.D., Lounejeva, E., Lyons, T.W., Sack, P.J., McGoldrick, P.J., Calver, C.R., 2014. Trace element content of sedimentary pyrite as a new proxy for deep-time ocean–atmosphere evolution. Earth Planet. Sci. Lett. 389, 209–220. https://doi.org/10.1016/j.epsl.2013.12.020.
Leube, A., Hirdes, W., Mauer, R., Kesse, G.O., 1990. The early Proterozoic Birimian Supergroup of Ghana and some aspects of its associated gold mineralization. Precambrian Res. 46 (1–2), 139–165. https://doi.org/10.1016/0301-9268(90)90070-7.
Ludwig, K.R., 2008. Isoplot 3.70: A Geochronological Toolkit for Microsoft Excel, 4. Berkeley Geochronology Center Special Publication.
Lyons, T.W., Reinhard, C.T., Planavsky, N.J., 2014. The rise of oxygen in Earth's early ocean and atmosphere. Nature 506 (7488), 307–315. https://doi.org/10.1038/nature13068.
Manceau, A., Lanson, M., Geoffroy, N., 2007. Natural speciation of Ni, Zn, Ba, and as in ferromanganese coatings on quartz using X-ray fluorescence, absorption, and diffraction. Geochim. Cosmochim. Acta 71 (1), 95–128. https://doi.org/10.1016/j.gca.2006.08.036.
Markwitz, V., Hein, K.A., Miller, J., 2016. Compilation of West African mineral deposits: spatial distribution and mineral endowment. Precambrian Res. 274, 61–81. https://doi.org/10.1016/j.precamres.2015.05.028.
Maynard, J.B., 2010. The chemistry of manganese ores through time: a signal of increasing diversity of earth-surface environments. Econ. Geol. 105 (3), 535–552. https://doi.org/10.2113/gsecongeo.105.3.535.
McManus, J., Nägler, T.F., Siebert, C., Wheat, C.G., Hammond, D.E., 2002. Oceanic molybdenum isotope fractionation: diagenesis and hydrothermal ridge-flank alteration. Geochem. Geophys. Geosyst. 3 (12), 1078. https://doi.org/10.1029/2002GC000356.
Meister, P., Bernasconi, S.M., Aiello, I.W., Vasconcelos, C., Mckenzie, J.A., 2009. Depth and controls of Ca-rhodochrosite precipitation in bioturbated sediments of the Eastern Equatorial Pacific, ODP Leg 201, Site 1226 and DSDP Leg 68, Site 503. Sedimentology 56 (5), 1552–1568. https://doi.org/10.1111/j.1365-3091.2008.01046.x.
Melcher, F., 1995. Genesis of chemical sediments in Birimian greenstone belts: evidence from gondites and related manganese-bearing rocks from northern Ghana. Mineral. Mag. 59 (2), 229–251. https://doi.org/10.1180/minmag.1995.059.395.08.
Melezhik, V.A., Huhma, H., Condon, D.J., Fallick, A.E., Whitehouse, M.J., 2007. Temporal constraints on the Paleoproterozoic Lomagundi-Jatuli carbon isotopic event. Geology 35 (7), 655–658. https://doi.org/10.1130/G23764A.1.

Miller, C.A., Peucker-Ehrenbrink, B., Walker, B.D., Marcantonio, F., 2011. Re-assessing the surface cycling of molybdenum and rhenium. Geochim. Cosmochim. Acta 75 (22), 7146–7179. https://doi.org/10.1016/j.gca.2011.09.005.

Mucci, A., 2004. The behavior of mixed Ca–Mn carbonates in water and seawater: controls of manganese concentrations in marine porewaters. Aquat. Geochem. 10 (1–2), 139–169. https://doi.org/10.1023/B:AQUA.0000038958.56221.b4.

Mücke, A., Dzigbodi-Adjimah, K., Annor, A., 1999. Mineralogy, petrography, geochemistry and genesis of the Paleoproterozoic Birimian manganese-formation of Nsuta/Ghana. Mineral. Deposita 34 (3), 297–311. https://doi.org/10.1007/s001260050205.

Nägler, T.F., Neubert, N., Böttcher, M.E., Dellwig, O., Schnetger, B., 2011. Molybdenum isotope fractionation in pelagic euxinia: evidence from the modern Black and Baltic Seas. Chem. Geol. 289 (1–2), 1–11. https://doi.org/10.1016/j.chemgeo.2011.07.001.

Nakagawa, Y., Takano, S., Firdaus, M.L., Norisuye, K., Hirata, T., Vance, D., Sohrin, Y., 2012. The molybdenum isotopic composition of the modern ocean. Geochem. J. 46 (2), 131–141. https://doi.org/10.2343/geochemj.1.0158.

Noda, N., Imamura, S., Sekine, Y., Kurisu, M., Fukushi, K., Terada, N., Uesugi, S., Numako, C., Takahashi, Y., Hartmann, J., 2019. Highly oxidizing aqueous environments on early Mars inferred from scavenging pattern of trace metals on manganese oxides. J. Geophys. Res.: Planets 124. https://doi.org/10.1029/2018JE005892.

Noordmann, J., Weyer, S., Montoya-Pino, C., Dellwig, O., Neubert, N., Eckert, S., Paetzel, M., Böttcher, M.E., 2015. Uranium and molybdenum isotope systematics in modern euxinic basins: Case studies from the Central Baltic Sea and the Kyllaren fjord (Norway). Chem. Geol. 396, 182–195. https://doi.org/10.1016/j.chemgeo.2014.12.012.

Nyame, F.K., 2008. Petrography and geochemistry of intraclastic manganese–carbonates from the ~2.2 Ga Nsuta deposit of Ghana: significance for manganese sedimentation in the Palaeoproterozoic of West Africa. J. Afr. Earth Sci. 50 (2–4), 133–147. https://doi.org/10.1016/j.jafrearsci.2007.09.007.

Nyame, F.K., 2013. Origins of Birimian (ca 2.2 G a) mafic magmatism and the Paleoproterozoic 'greenstone belt' metallogeny: a review. Island Arc 22 (4), 538–548. https://doi.org/10.1111/iar.12047.

Nyame, F.K., Kase, K., Yamamoto, M., 1998. Spessartine garnets in a manganiferous carbonate formation from Nsuta, Ghana. Resour. Geol. 48 (1), 13–22. https://doi.org/10.1111/j.1751-3928.1998.tb00003.x.

Nyame, F.K., Beukes, N.J., Kase, K., Yamamoto, M., 2003. Compositional variations in manganese carbonate micronodules from the lower Proterozoic Nsuta deposit, Ghana: product of authigenic precipitation or post-formational diagenesis? Sediment. Geol. 154 (3–4), 159–175. https://doi.org/10.1016/S0037-0738(02)00128-8.

Oberthür, T., Vetter, U., Davis, D.W., Amanor, J.A., 1998. Age constraints on gold mineralization and Paleoproterozoic crustal evolution in the Ashanti belt of southern Ghana. Precambrian Res. 89 (3–4), 129–143. https://doi.org/10.1016/S0301-9268(97)00075-2.

Ossa Ossa, F., Hofmann, A., Wille, M., Spangenberg, J.E., Bekker, A., Poulton, S.W., Eickmann, B., Schoenberg, R., 2018. Aerobic iron and manganese cycling in a redox-stratified Mesoarchean epicontinental sea. Earth Planet. Sci. Lett. 500, 28–40. https://doi.org/10.1016/j.epsl.2018.07.044.

Partin, C.A., Bekker, A., Planavsky, N.J., Scott, C.T., Gill, B.C., Li, C., Podkovyrov, V., Maslov, A., Konhauser, K.O., Lalonde, S.V., Love, G.D., Poulton, S.W., Lyons, T.W., 2013. Large-scale fluctuations in Precambrian atmospheric and oceanic oxygen levels from the record of U in shales. Earth Planet. Sci. Lett. 369–370, 284–293. https://doi.org/10.1016/j.epsl.2013.03.031.

Peucker-Ehrenbrink, B., Jahn, B.M., 2001. Rhenium-osmium isotope systematics and platinum group element concentrations: Loess and the upper continental crust. Geochem. Geophys. Geosyst. 2 (10) https://doi.org/10.1029/2001GC000172.

Peucker-Ehrenbrink, B., Ravizza, G., Hofmann, A.W., 1995. The marine $^{187}Os/^{186}Os$ record of the past 80 million years. Earth Planet. Sci. Lett. 130 (1–4), 155–167. https://doi.org/10.1016/0012-821X(95)00003-U.

Planavsky, N.J., Bekker, A., Hofmann, A., Owens, J.D., Lyons, T.W., 2012. Sulfur record of rising and falling marine oxygen and sulfate levels during the Lomagundi event. Proc. Natl. Acad. Sci. U. S. A. 109 (45), 18300–18305. https://doi.org/10.1073/pnas.1120387109.

Planavsky, N.J., Asael, D., Hofmann, A., Reinhard, C.T., Lalonde, S.V., Knudsen, A., Wang, X., Ossa Ossa, F., Pecoits, E., Smith, A.J.B., Beukes, N.J., Bekker, A., Johnson, T.M., Konhauser, K.O., Lyons, T.W., Rouxel, O.J., 2014. Evidence for oxygenic photosynthesis half a billion years before the Great Oxidation Event. Nat. Geosci. 7, 283–286. https://doi.org/10.1038/ngeo2122.

Planavsky, N.J., Slack, J.F., Cannon, W.F., O'Connell, B., Isson, T.T., Asael, D., Jackson, J.C., Hardisty, D.S., Lyons, T.W., Bekker, A., 2018. Evidence for episodic oxygenation in a weakly redox-buffered deep mid-Proterozoic Ocean. Chem. Geol. 483, 581–594. https://doi.org/10.1016/j.chemgeo.2018.03.028.

Polgári, M., Hein, J.R., Vígh, T., Szabó-Drubina, M., Fórizs, I., Bíró, L., Müller, A., Tóth, A.L., 2012. Microbial processes and the origin of the Úrkút manganese deposit, Hungary. Ore Geol. Rev. 47, 87–109. https://doi.org/10.1016/j.oregeorev.2011.10.001.

Poulson Brucker, R.L., McManus, J., Severmann, S., Berelson, W.M., 2009. Molybdenum behavior during early diagenesis: insights from Mo isotopes. Geochem. Geophys. Geosyst. 10 (6), Q06010 https://doi.org/10.1029/2008GC002180.

Poulson, R.L., Siebert, C., McManus, J., Berelson, W.M., 2006. Authigenic molybdenum isotope signatures in marine sediments. Geology 34 (8), 617–620. https://doi.org/10.1130/G22485.1.

Romaniello, S.J., Herrmann, A.D., Anbar, A.D., 2016. Syndepositional diagenetic control of molybdenum isotope variations in carbonate sediments from the Bahamas. Chem. Geol. 438, 84–90. https://doi.org/10.1016/j.chemgeo.2016.05.019.

Roy, S., 2006. Sedimentary manganese metallogenesis in response to the evolution of the Earth system. Earth Sci. Rev. 77 (4), 273–305. https://doi.org/10.1016/j.earscirev.2006.03.004.

Runnegar, B., 1991. Precambrian oxygen levels estimated from the biochemistry and physiology of early eukaryotes. Palaeogeogr. Palaeoclimatol. Palaeoecol. 97 (1–2), 97–111. https://doi.org/10.1016/0031-0182(91)90186-U.

Sawaki, Y., Moussavou, M., Sato, T., Suzuki, K., Ligna, C., Asanuma, H., Sakata, S., Obayashi, H., Hirata, T., Edou-Minko, A., 2017. Chronological constraints on the Paleoproterozoic Francevillian Group in Gabon. Geosci. Front. 8 (2), 397–407. https://doi.org/10.1016/j.gsf.2016.10.001.

Scott, C., Lyons, T.W., 2012. Contrasting molybdenum cycling and isotopic properties in euxinic versus non-euxinic sediments and sedimentary rocks: refining the paleoproxies. Chem. Geol. 324–325, 19–27. https://doi.org/10.1016/j.chemgeo.2012.05.012.

Scott, C., Lyons, T.W., Bekker, A., Shen, Y.A., Poulton, S.W., Chu, X.L., Anbar, A.D., 2008. Tracing the stepwise oxygenation of the Proterozoic Ocean. Nature 452 (7186), 456–459. https://doi.org/10.1038/nature06811.

Sekine, Y., Tajika, E., Tada, R., Hirai, T., Goto, K.T., Kuwatani, T., Goto, K., Yamamoto, S., Tachibana, S., Isozaki, Y., Kirschvink, J.L., 2011. Manganese enrichment in the Gowganda Formation of the Huronian Supergroup: a highly oxidizing shallow-marine environment after the last Huronian glaciation. Earth Planet. Sci. Lett. 307 (1–2), 201–210. https://doi.org/10.1016/j.epsl.2011.05.001.

Selby, D., Creaser, R.A., 2003. Re–Os geochronology of organic rich sediments: an evaluation of organic matter analysis methods. Chem. Geol. 200, 225–240. https://doi.org/10.1016/S0009-2541(03)00199-2.

Shaw, T.J., Gieskes, J.M., Jahnke, R.A., 1990. Early diagenesis in differing depositional environments: the response of transition metals in pore water. Geochim. Cosmochim. Acta 54 (5), 1233–1246. https://doi.org/10.1016/0016-7037(90)90149-F.

Siebert, C., Nägler, T.F., von Blanckenburg, F., Kramers, J.D., 2003. Molybdenum isotope records as a potential new proxy for paleoceanography. Earth Planet. Sci. Lett. 211 (1–2), 159–171. https://doi.org/10.1016/S0012-821X(03)00189-4.

Siebert, C., McManus, J., Bice, A., Poulson, R., Berelson, W.M., 2006. Molybdenum isotope signatures in continental margin marine sediments. Earth Planet. Sci. Lett. 241 (3–4), 723–733. https://doi.org/10.1016/j.epsl.2005.11.010.

Takahashi, Y., Manceau, A., Geoffroy, N., Marcus, M.A., Usui, A., 2007. Chemical and structural control of the partitioning of Co, Ce, and Pb in marine ferromanganese oxides. Geochim. Cosmochim. Acta 71 (4), 984–1008. https://doi.org/10.1016/j.gca.2006.11.016.

Waldbauer, J.R., Newman, D.K., Summons, R.E., 2011. Microaerobic steroid biosynthesis and the molecular fossil record of Archean life. Proc. Natl. Acad. Sci. U. S. A. 108 (33), 13409–13414. https://doi.org/10.1073/pnas.1104160108.

Wasylenki, L.E., Rolfe, B.A., Weeks, C.L., Spiro, T.G., Anbar, A.D., 2008. Experimental investigation of the effects of temperature and ionic strength on Mo isotope fractionation during adsorption to manganese oxides. Geochim. Cosmochim. Acta 72 (24), 5997–6005. https://doi.org/10.1016/j.gca.2008.08.027.

Wheat, C.G., Mottl, M.J., 2000. Composition of pore and spring waters from Baby Bare: Global implications of geochemical fluxes from a ridge flank hydrothermal system. Geochim. Cosmochim. Acta 64 (4), 629–642. https://doi.org/10.1016/S0016-7037(99)00347-6.

Willbold, M., Elliott, T., 2017. Molybdenum isotope variations in magmatic rocks. Chem. Geol. 449, 253–268. https://doi.org/10.1016/j.chemgeo.2016.12.011.

Yeh, H.W., Hein, J.R., Bolton, B.R., 1995. Origin of the Nsuta manganese carbonate proto-ore, Ghana: carbon-and oxygen-isotope evidence. J. Geol. Soc. China 38, 397–410.